Acoustic-phonon propagation in superlattices

S. Tamura,* D. C. Hurley, and J. P. Wolfe
Department of Physics and Materials Research Laboratory, University of Illinois at Urbana-Champaign, 104 South Goodwin Avenue, Urbana, Illinois 61801
(Received 8 October 1987)

Bragg reflection of acoustic phonons propagating through a periodic superlattice is explored in detail. We examine Bragg reflection for a single vibrational mode and relate it to gaps, or stop bands, in the phonon dispersion relation at the center and boundary of the folded Brillouin zone. Bragg reflection due to the coupling of different polarization modes is similarly linked to intrazone stop bands. We also calculate phonon transmission rates, and explore in depth the spatial distribution of the transmitted phonon intensity. These results are compared with experimental phonon images that provide a two-dimensional map of the acoustic-phonon transmission as a function of propagation direction.

I. INTRODUCTION

With the perfection of thin-film techniques that enable high-quality, crystalline multilayer structures—superlattices (SL's)—to be produced, research exploring the various properties of such systems has boomed. Of great interest is the artificial periodicity of a SL, much longer than the atomic spacing, imposed by alternating layers of different materials. In addition to extensive investigation of the electronic quantum states and transport properties, there have been a number of studies which explored the vibrational characteristics of SL's.[1-14] One of the most fundamental acoustic properties of a SL is the Bragg reflection of long-wavelength phonons. The condition for Bragg reflection requires $m\lambda = 2D\cos\theta$, where λ is the phonon wavelength, D is the superlattice period, θ is the phonon wave-vector angle of incidence measured from the normal of the interfaces, and m is an integer. Phonons satisfying this condition are Bragg-reflected from an ideal SL. This Bragg reflection produces band gaps, or "stop bands," at the boundary and center of the folded Brillouin zone.

Previous works have shown that Bragg reflection in SL's results in dips in the phonon transmission as a function of frequency.[10,11] The well-known stop bands at the boundary and center of the folded Brillouin zone are a direct result of Bragg scattering. The reflection of zone-center and zone-edge phonons has been observed experimentally for both crystalline[10,12] and amorphous systems.[11,14] The first experiments involved phonon propagation perpendicular to the interfaces, in a direction of high crystalline symmetry, or else in an isotropic (amorphous) system. Using the phonon-imaging technique, we have recently observed the zone-boundary stop bands and also stop bands *within* the zone due to mode coupling of phonons propagating in off-symmetry directions.[12] These frequency gaps were predicted theoretically[13] and are attributed to a generalized form of intermode Bragg reflection. The coupled-mode stop bands in SL's appear to be a phenomenon unique to phonons, as contrasted to electromagnetic waves or electrons. Further evidence for their existence has recently been observed using phonon spectroscopy techniques.[14]

This paper systematically examines the issues concerned with the Bragg reflection of phonons in a SL for an arbitrary phonon propagation direction. We address in detail such topics as the influence of crystalline anisotropy on Bragg reflection, and how the standard Bragg condition is modified if the reflection involves mode conversion. The paper is organized to present the relevant physical concepts with gradually increasing theoretical and mathematical detail. In Sec. II we begin with the fundamental process of phonon propagation through SL's for the case of normal incidence. This restriction excludes the possibility of coupling between the different polarization modes. Such simplifications help to emphasize the physical principles involved. First, we calculate the dispersion relation for phonons at normal incidence to a SL. Next, we compute the phonon transmission through the SL. The discussion in Sec. III extends the topics of Sec. II to the more general question of phonon propagation through SL's for an arbitrary (oblique) angle of incidence, including the possibility of coupling between the modes. In Sec. IV we focus on the specific topic of the angular dependence of phonon transmission. To further elucidate this topic we present spatial maps of the Bragg condition as well as detailed Monte Carlo calculations of the spatial distribution of stop bands. Finally, in Sec. V these theoretical results are compared to data obtained in several phonon-imaging experiments.

II. BRAGG REFLECTION OF PHONONS FROM SUPERLATTICES (NORMAL INCIDENCE)

A. General considerations

We first consider the simplest case of acoustic phonons propagating through a SL perpendicular to the interfaces. Figure 1(a) depicts the ideal SL system under consideration. The system consists of an infinite repetition of alternating layers of material A with thickness d_A and material B with thickness d_B. Thus the SL period is $D = d_A + d_B$. The interfaces are parallel to the $\mathbf{x}_\parallel = (x_1, x_2)$ plane, with the z axis (x_3 axis) normal to the

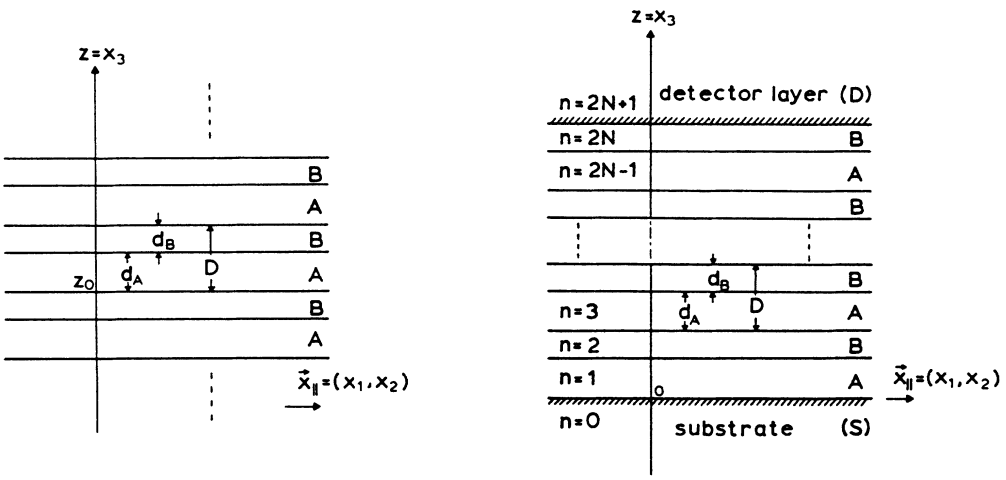

FIG. 1. Schematic superlattice (SL) systems. (a) Ideal (infinite) SL with alternating layers of materials A and B. The individual layer thicknesses are d_A and d_B, so that the SL periodicity is $D=d_A+d_B$. The layer interfaces lie in the $\mathbf{x}_\parallel=(x_1,x_2)$ plane perpendicular to the z axis (x_3 axis). (b) Real (finite) SL. Phonons originate in the substrate layer S (GaAs), propagate through N periods ($2N+1$ interfaces) of the SL, and are observed in the detector layer D.

interfaces. We consider phonons with wavelength λ propagating along the z axis (i.e., $\theta=0°$, where θ is the angle the wave vector makes with the z axis). In this case, the condition for Bragg reflection of the phonons is simply

$$m\lambda=2D \ , \tag{1}$$

where m is an integer. Since the basic reciprocal-superlattice vector has a magnitude $G_0=|\mathbf{G}_0|=2\pi/D$, an equivalent form of the Bragg condition is

$$2q=mG_0 \ , \tag{2}$$

where $q=2\pi/\lambda$ is the magnitude of the phonon wave vector in the SL. Hence, phonons with $q=q_m\equiv m\pi/D=mG_0/2$ are Bragg-reflected and cannot propagate through the SL.

It is important to notice that the simple Bragg-scattering condition, Eqs. (1) or (2), is valid for arbitrary thicknesses d_A and d_B. In the general case, the phonon displacement field is a modulated plane wave, $u(z)e^{iqz}$, where the modulation function satisfies the periodicity condition, $u(z+D)=u(z)$. This is the Floquet or Bloch theorem. The local phase of the wave in one layer of medium A, for example, can be described by a wave vector $k_A=\omega/v_A$, but there is no simple relation among q, k_A, and k_B. Of course, $\omega=k_Av_A=k_Bv_B$, where v_A and v_B are wave velocities in the respective media. Below we will write down the dispersion relation for q in terms of ω, d_A, d_B, v_A, and v_B.

A schematic of the extended-zone scheme in Fig. 2 indicates q vectors for which the Bragg condition is satisfied, namely those equal to reciprocal vectors $m\mathbf{G}_0$. Thus, the wave number q defines the folded Brillouin zone $-\pi/D\le q\le\pi/D$, and $q=q_m$ correspond to the center and boundaries of the zone. As in the phonon dispersion relation for bulk materials, we expect frequency gaps to occur at the boundaries of the reduced zone. The difference in acoustic impedance of the two adjacent layers results in two vibrational modes of the same wavelength, but different frequencies. As a result, gaps in frequency—or "phonon stop bands"—are formed at the zone boundary and zone center. Raman scattering has been used to investigate the dispersion relation close to the center of the folded zone.[2–5]

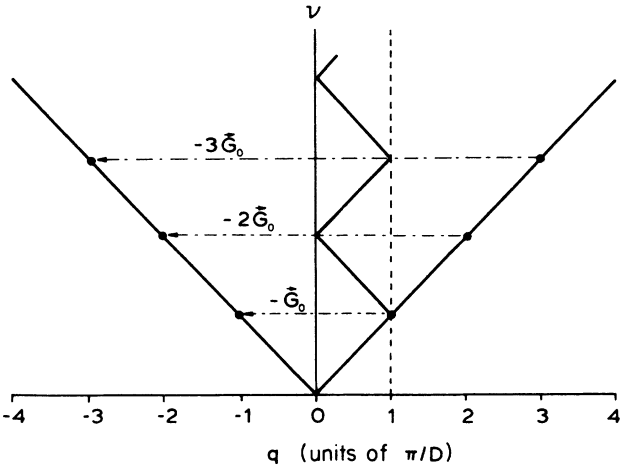

FIG. 2. (a) Schematic for Bragg reflection of phonons in the ν-q plane. Phonons with SL wave vector $q=q_m=m\pi/D$ ($m=1,2,\ldots$) are Bragg-reflected. Both the extended zone and half of a folded zone ($0\le q\le\pi/D$) are shown. The Bragg condition may also be written in terms of the reciprocal-SL vector $G_0=2\pi/D$ [Eq. (2) in text].

B. Phonon dispersion relation

With this qualitative picture in mind, we discuss a quantitative method to calculate the phonon dispersion relation for a specific SL. The SL system is as described in Fig. 1(a). Although the dispersion relation for phonon propagation perpendicular to the SL interfaces has already been published,[6] it is worthwhile to briefly repeat the derivation in order to establish the notation for the more general cases of propagation developed later. Here we assume that the interfaces are the mirror-symmetry planes of the crystal and therefore all three modes of the phonons are decoupled from each other for normal propagation.

Let U be the lattice displacement of a given mode. In each SL layer, U takes the form

$$U_I(z)=a_I^t e^{ik_I z}+a_I^r e^{-ik_I z} , \tag{3}$$

where $I=A$ or B identifies the layers, a^t and a^r represent the amplitudes of transmitted ($+z$ propagating) and reflected ($-z$ propagating) waves, and $k_I=\omega/v_I$ with v_I the sound velocity. The time dependence $e^{-i\omega t}$ of U has been suppressed in Eq. (3) to simplify the notations introduced below. Now, the displacement U_I and the stress $S_I=\mu_I(\partial U_I/\partial z)$ (where μ_I is an appropriate elastic constant) must satisfy continuity and periodicity conditions in the SL. The continuity condition is simply

$$f_A(z_0)=f_B(z_0) , \tag{4}$$

where $z=z_0$ is an interface [see Fig. 1(a)] and f_I represents both U_I and S_I. The periodicity condition is given by the Floquet theorem, which states

$$f_A(z_0+D)=e^{iqD}f_B(z_0) , \tag{5}$$

or, equivalently,

$$f_A(z_0+d_A)=e^{iqD}f_B(z_0-d_B) . \tag{5'}$$

We stress again that q is the SL wave number that describes the modulation of waves in the SL as a whole. Here it is convenient to introduce a 2×2 h matrix defined by

$$h_I(z)=\begin{bmatrix} e^{ik_I z} & e^{-ik_I z} \\ \mu_I k_I e^{ik_I z} & -\mu_I k_I e^{-ik_I z} \end{bmatrix} . \tag{6}$$

Then, using $z_0=0$ in Eqs. (4) and (5') leads to

$$\det\begin{bmatrix} h_A(0) & -h_B(0) \\ h_A(d_A) & -\chi h_B(-d_B) \end{bmatrix}=0 , \tag{7}$$

where $\chi=e^{iqD}$. Because, in general, $\det[h_A(0)]$ and $\det[h_B(-d_B)]\neq 0$, Eq. (7) may also be written as

$$\det(M-\chi E)=0 , \tag{8}$$

where $M\equiv h_A(d_A)[h_A(0)]^{-1}h_B(0)[h_B(-d_B)]^{-1}$ and E is a 2×2 unit matrix. Hence, χ is given by the eigenvalue of the matrix M.

By explicitly solving Eq. (8), we obtain the dispersion relation[6]

$$\cos(qD)=\cos\left[\frac{\omega d_A}{v_A}\right]\cos\left[\frac{\omega d_B}{v_B}\right] -\frac{1+\delta^2}{2\delta}\sin\left[\frac{\omega d_A}{v_A}\right]\sin\left[\frac{\omega d_B}{v_B}\right] , \tag{9}$$

where $\delta=\rho_A v_A/\rho_B v_B$ is the ratio of the acoustic impedances and ρ_I is the mass density of a layer. This equation may also be viewed as a relationship between the effective wave vector q of the SL as a whole and the wave vectors $k_I=\omega/v_I$ in the individual layers. The right-hand side of Eq. (9) is a continuous function of ω, and its modulus exceeds unity for some ranges of ω, whereas the left-hand side is bounded by -1 and 1. Therefore, frequency gaps exist for the general ω-versus-q relation. The gaps occur for those q producing an extremal value of $\cos(qD)$, i.e., $q=m\pi/D$, which coincides with the Bragg condition [Eq. (2)].

The width $\Delta\omega$ of the frequency gaps may be derived from a simple perturbation calculation. Note first that Eq. (9) can be rewritten as

$$\cos(qD)=\cos\left[\omega\left[\frac{d_A}{v_A}+\frac{d_B}{v_B}\right]\right] -\gamma\sin\left[\frac{\omega d_A}{v_A}\right]\sin\left[\frac{\omega d_B}{v_B}\right] , \tag{9'}$$

where $\gamma=(1-\delta)^2/2\delta$. Because δ is close to unity for most SL's, the second term on the right-hand side of Eq. (9') can be regarded as a small perturbation. At the mth-order Bragg scattering, $q=m\pi/D=q_m$, and we write $\omega=\omega_m+\Delta\omega_m/2$, where $\cos[\omega_m(d_A/v_A+d_B/v_B)]=(-1)^m$ and $\Delta\omega_m/\omega_m\ll 1$. Thus, for normal incidence and $\delta\approx 1$, the center of the mth-order frequency gap is given by

$$\omega_m=m\pi/(d_A/v_A+d_B/v_B) , \tag{10}$$

and, by substitution into Eq. (9'), the width of this gap is found to be

$$\Delta\omega_m=\frac{2}{d_A/v_A+d_B/v_B}(2\gamma)^{1/2} \times\left|\sin\left[\frac{\omega_m d_A}{v_A}\right]\sin\left[\frac{\omega_m d_B}{v_B}\right]\right|^{1/2} . \tag{10'}$$

For $d_A=d_B$, $\sin(\omega_m d_A/v_A)$ is nearly zero at the zone center, whereas at the zone boundary it is close to unity. Therefore, in this case, $\Delta\omega_m$ at the zone center is small compared to its value at the zone boundary.

Figure 3(a) shows the dispersion relation for phonons in an AlAs/GaAs SL with $D/2=d_A=d_B$.[15] As expected, stop bands occur for phonon wave vectors at the center and edge of the Brillouin zone. Moreover, the zone-center stop bands are quite small. We also note that $d\omega/dq=0$ at $q=q_m$ ($m\neq 0$). As $\omega\to 0$, the phonon wavelength becomes much longer than the SL periodicity, becoming a bulk sound wave with a linear dispersion relation with slope given by

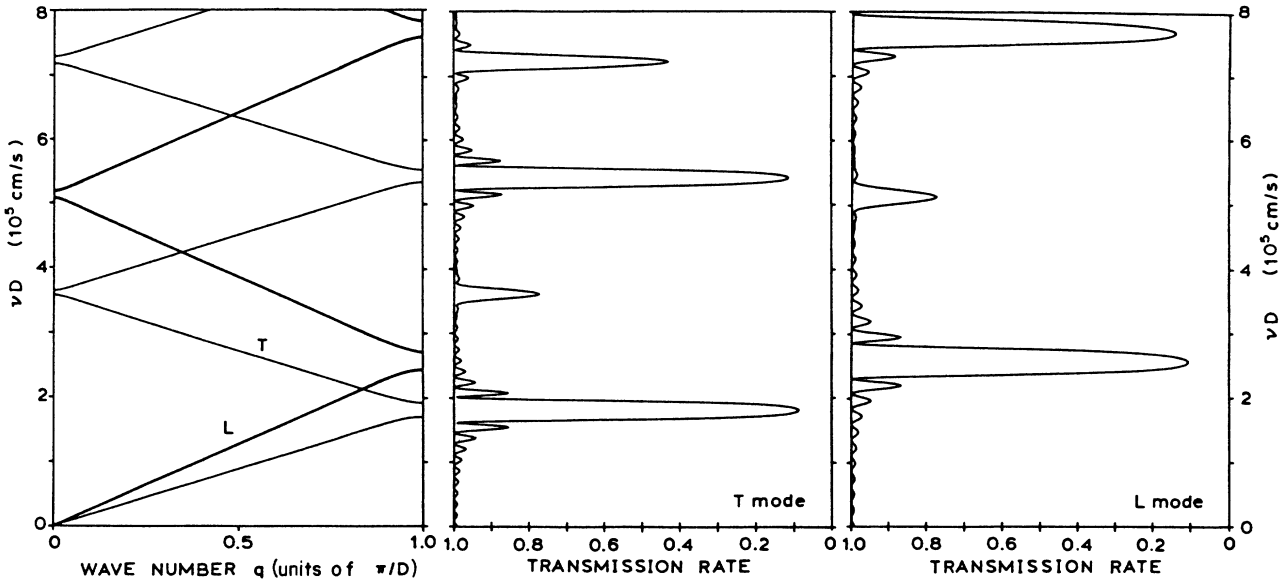

FIG. 3. (a) Dispersion relation for phonons at normal incidence to an infinite AlAs/GaAs SL with $d_A = d_B = D/2$. Stop bands occur at the folded Brillouin-zone center and boundary ($q = \pi/D$). (b) Transmission rate vs the product νD for transverse (T) phonons at normal incidence in an (001) AlAs/GaAs SL with 15 periods. Transmission rate is defined as (transmitted flux)/(incident flux), as discussed in the text. Transmission dips occur for frequencies that satisfy the intramode Bragg reflection condition, i.e., frequencies in the T-mode stop bands. (c) Transmission vs νD for longitudinal (L) phonons, with similar attenuation due to L stop bands.

$$c \equiv \frac{\omega}{q} = D \left[\left[\frac{d_A}{v_A} \right]^2 + \left[\frac{d_B}{v_B} \right]^2 + \frac{1+\delta^2}{\delta} \frac{d_A d_B}{v_A v_B} \right]^{-1/2} . \tag{11}$$

C. Transmission rates

We now calculate the transmission rate of phonons propagating through a finite-period SL. We continue to consider normal incidence, which precludes the possibility of mode conversion. In this system the exact periodicity perpendicular to the interfaces is absent, so Eq. (5) is no longer valid. However, Eq. (4) remains valid as the continuity condition of the displacement and stress fields at each interface.

In the situation under consideration, phonons of a given mode (with unit amplitude) are incident on the SL from the substrate (denoted by S), then propagate through N periods ($2N+1$ interfaces) to reach a detector layer (D). This system is shown in Fig. 1(b). In the substrate there exists one $+z$-propagating (incident) wave and one $-z$-propagating (reflected) wave, while in the detector layer there is only a $+z$-propagating wave. A two-component column vector $\mathbf{w}$ can be defined consisting of the two displacement amplitudes in each SL layer:

$$\mathbf{w}_n = \begin{bmatrix} a_n^t \\ a_n^r \end{bmatrix} . \tag{12}$$

Here the layers are identified by the index n instead of I ($= A$ or B), which denotes the layer number ordered from $n=0$ to $n=2N+1$. (It should be remarked that odd n corresponds to $I=A$ and even n to $I=B$, as in Fig. 1(b). So the suffix n is more general than I.) Note that we assume $a_{2N+1}^r = 0$ for the detector layer and $a_0^t = 1$ for the substrate. Using the 2×2 h matrix of Eq. (6) and $\mathbf{w}$, it is convenient to express the continuity condition [Eq. (4)] of the displacement and stress fields at the interfaces as

$$\begin{aligned} h_s(0)\mathbf{w}_0 &= h_A(0)\mathbf{w}_1, \\ h_A(d_A)\mathbf{w}_1 &= h_B(d_A)\mathbf{w}_2, \\ &\vdots \\ h_A(ND-d_B)\mathbf{w}_{2N-1} &= h_B(ND-d_B)\mathbf{w}_{2N}, \\ h_B(ND)\mathbf{w}_{2N} &= h_D(ND)\mathbf{w}_{2N+1} . \end{aligned} \tag{13}$$

Elimination of the intermediate vectors $\mathbf{w}_1 - \mathbf{w}_{2N}$ from Eq. (13) yields a relation between the substrate phonon wave amplitudes $\mathbf{w}_S = \mathbf{w}_0$ and the detector-layer phonon wave amplitudes $\mathbf{w}_D = \mathbf{w}_{2N+1}$:

$$\mathbf{w}_D = T\mathbf{w}_S , \tag{14}$$

where the "transfer matrix" T is given by

$$T=[h_D(ND)]^{-1}h_B(ND)[h_B(ND-d_B)]^{-1}h_A(ND-d_B)\cdots[h_A(0)]^{-1}h_S(0)\ . \tag{15}$$

Solution of Eq. (14) yields the amplitudes a_D^t of the transmitted wave in the detector and a_S^r of the reflected wave in the substrate.

The transmission rate is defined as the transmitted energy flux of the phonons reaching the detector layer normalized by the energy flux of the incident wave in the substrate. The energy flux is given by

$$P_I=\tfrac{1}{2}\rho_I\omega^2V_I\,|\,a_I^t\,|^2\ . \tag{16}$$

In this equation V_I is the group velocity of the wave. For normal incidence and in the continuum approximation, $V_I=v_I$. Since $a_S^t=1$, the transmission rate is

$$\frac{P_D}{P_S}=\frac{\rho_D v_D}{\rho_S v_S}\,|\,a_D^t\,|^2\ . \tag{17}$$

Figures 3(b) and 3(c) show the calculated transmission rates of longitudinal (L) and transverse (T) phonons propagating through a GaAs substrate into a (001) AlAs/GaAs SL with 15 periods. Here we have assumed $d_A=d_B=D/2$ and a perfect acoustic match between the SL and detector layer. The plots reveal several prominent dips in transmission that occur at the frequency gaps in the dispersion relations. One can see a correlation between the width of the frequency gaps and the magnitude of the transmission dips. If the number of SL periods is increased, the relatively shallow dips become deeper. Increasing the number of periods also increases the number of small oscillations in the transmission rate, which are caused by interference effects between the transmitted and reflected waves.

We note here that the graphs in Figs. 3(b) and 3(c) are exactly the type used to analyze the results of previous experiments. Dips in the acoustic-phonon transmission for normal incidence were first observed experimentally by Narayanamurti *et al.*[10] in crystalline $Ga_{1-x}Al_xAs/GaAs$ superlattices and more recently by Koblinger *et al.*[11] in amorphous SiO_2/Si superlattices. Both studies made use of the phonon spectroscopy technique, which measures the time-integrated phonon intensity as a function of frequency. The observed transmission dips can be correlated to the Bragg reflection of phonons with frequencies $\nu=\nu_m=m\pi c/D$ [c given by Eq. (11)] corresponding to the mth-order reflection. In each case, simulations of the transmission rate based on the transfer-matrix method supported the idea that the attenuation observed was due to the first- or second-order (zone-edge or zone-center) stop bands.

III. GENERAL THEORY OF ACOUSTIC-PHONON PROPAGATION IN SUPERLATTICES

This section parallels the development of Sec. II for the case of a phonon incident on the SL at an arbitrary angle. Again it is assumed that the normal to the SL interfaces is a twofold or fourfold crystalline symmetry axis. Oblique incidence immediately introduces several complications, but as we shall see, these complications give the phonon-SL interaction its unique properties. For $\theta\neq0°$ it is generally impossible to decouple the different polarization modes, so all three phonon modes must be handled simultaneously. For oblique propagation directions, the polarization modes are not pure, but instead contain both L and T components. At each interface, an incident wave therefore may be reflected or transmitted into any of the three modes; the relative amplitudes of the reflected and transmitted waves for each mode will vary (perhaps dramatically) as a function of θ. The principles of Sec. II are extended to account for these conditions.

A. Oblique incidence and intermode Bragg reflection

If we temporarily ignore the possibility of mode conversion, the situation indicated in Fig. 4(a) exists. Phonons with wave vector $\mathbf{K}$ incident on a SL layer at an angle $\theta\neq0°$ are specularly reflected at the same angle. It is easy to extend the Bragg-reflection condition of Sec. II to give the standard Bragg condition for constructive interference at oblique incidence:

$$2D\cos\theta=m\lambda\ , \tag{18}$$

where $\cos\theta=\hat{\mathbf{K}}\cdot\hat{\mathbf{z}}$ and $\hat{\mathbf{z}}$ is a unit vector normal to the superlattice interface. Defining $\mathbf{K}=(\mathbf{k}_\parallel,q)$ and using the reciprocal-superlattice vector $\mathbf{G}_0$, Eq. (18) may be written in a form identical to Eq. (2). [Note that the SL wave vector $\mathbf{K}$ is different from the wave vector $\mathbf{k}=(\mathbf{k}_\parallel,k_z)$ in an individual layer, although the component $\mathbf{k}_\parallel$ parallel to the interface is common to $\mathbf{K}$ and $\mathbf{k}$.] It is important to remember that now q represents the wave-vector component *normal* to the interfaces. Therefore we expect zone-edge and zone-center stop bands similar to those in Fig. 3(a) to occur when the normal component of the wave vector is the appropriate value, given by Eq. (2).

Allowing for the possibility of mode conversion changes the situation to that indicated in Fig. 4(b). Comparison to Fig. 4(a) suggests that a generalized form of the Bragg condition for oblique incidence that includes the possibility of mode conversion can be written as (for L→T or vice versa)

$$D\left[\frac{\cos\theta_{\rm L}}{\lambda_{\rm L}}+\frac{\cos\theta_{\rm T}}{\lambda_{\rm T}}\right]=m\ , \tag{19}$$

where $\lambda_{\rm L}$ ($\lambda_{\rm T}$) and $\theta_{\rm L}$ ($\theta_{\rm T}$) are the wavelength and angle of incidence or reflection of the L (T) phonons. In terms of the normal components $q_{\rm L}$ and $q_{\rm T}$ of the L- and T-phonon wave vectors, the Bragg condition becomes

$$q_{\rm L}+q_{\rm T}=mG_0\ . \tag{20}$$

Simultaneously, conservation of the phonon frequency and wave vector parallel to the interface must be satisfied, i.e., $\nu_{\rm L}=\nu_{\rm T}$ and $\mathbf{k}_\parallel^{\rm L}=\mathbf{k}_\parallel^{\rm T}$. In an anisotropic medium with two distinct T branches, intermode Bragg reflection between the T modes is also possible.

Figure 5 shows the processes of T to L Bragg reflection

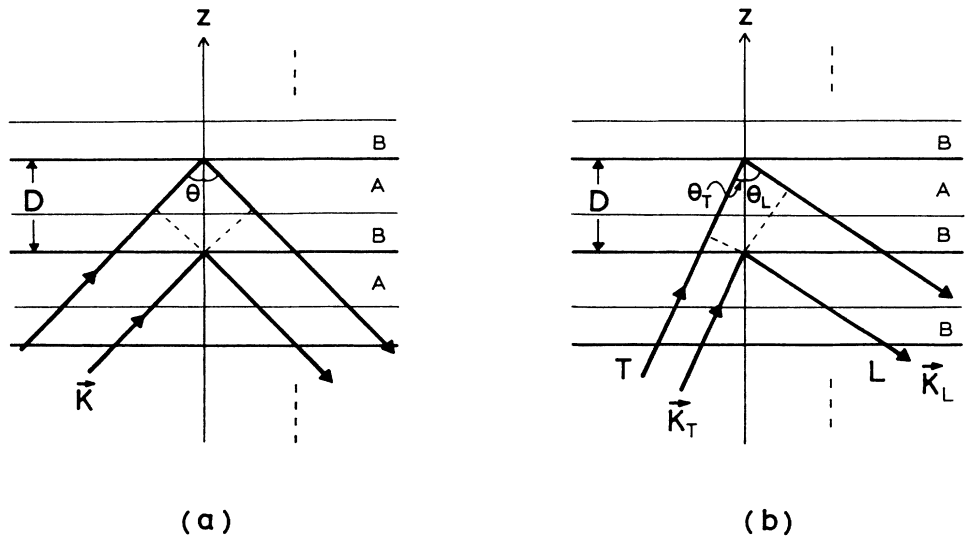

FIG. 4. (a) Schematic of Bragg reflection for phonons at an oblique angle of incidence θ to a SL. Mode conversion between different polarizations is not considered. (b) Schematic of intermode Bragg reflection at oblique incidence in which the different polarization modes couple.

in the ν-q plane. In the folded Brillouin zone, intermode reflections occur where the folded dispersion curves of the L and T modes intersect (open circles). As we shall see, the coupling between modes at these points produces an "anticrossing," or "coupled-mode stop band." This effect is not observed in the normal-incidence case (Fig. 3) because the L and T waves have orthogonal polarizations.

B. Slowness surface and transmitted and reflected wave vectors at a single interface

Before calculating the dispersion relations for phonons propagating obliquely in a SL, we must consider the processes of transmission and reflection at a single interface.[16] Figure 6 shows the (100) sections of the slowness surfaces for each half of the AlAs/GaAs interface. These surfaces represent a polar plot of the wave-vector amplitude at a constant frequency ω_0; that is,

$$|\mathbf{k}_I| = \frac{\omega_0}{v(\mathbf{k}_I)} , \tag{21}$$

where $v(\mathbf{k}_I)$ is the phase velocity in layer I. The slowness surface has one sheet for each of the three modes [L, FT (fast transverse), and ST (slow transverse)]. It is not spherical (and the transverse modes are not degenerate) due to the elastic anisotropy of the crystals.

The slowness surface reveals the anisotropy of the phase velocity v. Moreover, since the group velocity $\mathbf{V}=\nabla_k\omega$ is normal to the surface, this construction makes it clear that $\mathbf{k}$ and $\mathbf{V}$ are not, in general, parallel. This property of all crystals can produce an extremely anisotropic phonon flux intensity emanating from a point source of heat—an effect known as "phonon focusing."[17]

The cross sections of the slowness surfaces plotted in Fig. 6 indicate the restrictions that exist on the transmitted and reflected wave-vector components for a given incident $\mathbf{k}$ vector. Conservation of $k_\parallel = |\mathbf{k}_\parallel|$ across the flat interface restricts the choice of reflected and transmitted $\mathbf{k}$ vectors. For the value of $\mathbf{k}_\parallel$ indicated in Fig. 6(a), there are six real $\mathbf{k}$'s satisfying Eq. (21). Among them three solutions represent $+z$-propagating waves, and the other three are $-z$-propagating waves. As Fig. 6(b) demonstrates, for certain values of $\mathbf{k}_\parallel$ it is possible that no real $\mathbf{k}$ satisfying Eq. (21) exists for a certain mode (sheet). In this case an evanescent wave is formed for that mode. As we shall see in the discussion below, this indicates an imaginary solution of the wave equation for the normal component of k_z of $\mathbf{k}$.

The plane-wave solution of the phonon displacement vector $\mathbf{U}$ in a particular SL layer is

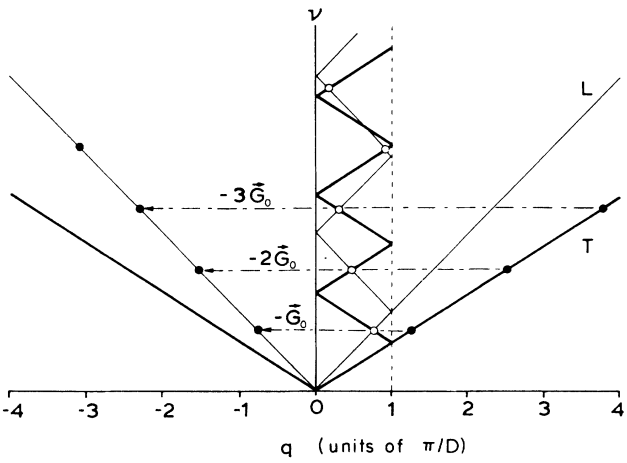

FIG. 5. Schematic of intermode Bragg reflection in the ν-q plane. For oblique angles of incidence, phonons of different polarizations couple if the sum of their normal wave-vector components q_L and q_T are an integral number of reciprocal-SL wave vectors G_0 [Eq. (20)]. The coupling causes an "anticrossing" or intramode stop bands in the dispersion relation (open circles).

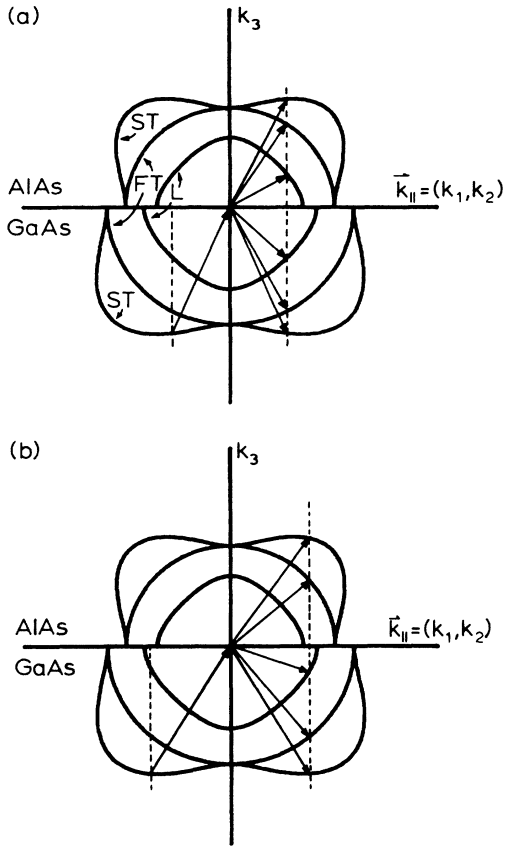

FIG. 6. Cross sections in the (100) plane of the slowness (constant-frequency) surfaces for a GaAs/AlAs interface. Each slowness surface consists of three sheets corresponding to the three polarization modes (L, FT, and ST). (a) Phonons incident at the interface with the $k_\parallel=|\mathbf{k}_\parallel|=(k_1,k_2)$ indicated have six possible reflected and transmitted wave vectors that conserve $\mathbf{k}_\parallel$. (b) Phonons incident with this value of $\mathbf{k}_\parallel$ cannot conserve $\mathbf{k}_\parallel$ for L phonons in AlAs, so an evanescent L wave is formed.

$$\mathbf{U}(\mathbf{r})=a\boldsymbol{\varepsilon}e^{-i\omega t+i\mathbf{k}\cdot\mathbf{r}}\ , \tag{22}$$

where $\mathbf{r}=(\mathbf{x}_\parallel,z)$, a is an amplitude, and $\boldsymbol{\varepsilon}$ is a polarization vector. (For the moment we will suppress the index I in U for simplicity.) Note that the phonon displacement U treated in Sec. II is a scalar, but now we require a vector $\mathbf{U}$ with three Cartesian coordinates. The wave equation for $\mathbf{U}$ must satisfy the Christoffel equation,[18]

$$(C_{ilmn}k_lk_n-\rho\omega^2\delta_{im})\varepsilon_m=0\ , \tag{23}$$

where C_{ilmn} is the elastic-constant tensor of the layer. Since the secular equation

$$\det(C_{ilmn}k_lk_n-\rho\omega^2\delta_{im})=0 \tag{24}$$

is of degree 6 in $\mathbf{k}$, in each layer there are six solutions $k_z^{(j)}$, $j=1,2,\ldots,6$ for any initial values of $\mathbf{k}_\parallel$ and ω. For small $\mathbf{k}_\parallel$, all of the k_z are real, as can be seen from Fig. 6(a). Three of the solutions (those with $k_z>0$) correspond to the $+z$-propagating bulk wave for each mode, and three (those with $k_z<0$) correspond to the $-z$-propagating bulk waves. Thus the total displacement vector in a layer takes the form

$$\mathbf{U}=e^{-i\omega t}e^{i\mathbf{k}_\parallel\cdot\mathbf{x}_\parallel}\sum_{j=1}^{6}a^{(j)}\boldsymbol{\varepsilon}^{(j)}e^{ik_z^{(j)}z}\ . \tag{25}$$

Note that j is an index over both the phonon mode ($j=1,2,3$) and the reflected or transmitted character (r and t) of the mode. For larger values of $\mathbf{k}_\parallel$, some solutions to Eq. (24) will be complex [see Fig. 6(b)]. (The imaginary solutions occur as complex-conjugate pairs.) Equation (25) indicates that imaginary values of k_z correspond to inhomogeneous waves, i.e., evanescent waves, that exponentially rise or fall in amplitude toward the interior of the medium. Nonetheless, there are always six waves of some kind in each layer.

The phonon displacement vector $\mathbf{U}$ produces the stress vector $\mathbf{S}$ (in interfaces which are normal to $z=x_3$) defined by

$$\begin{aligned}S_l&=C_{3lmn}\partial_m U_m\\&\equiv e^{-i\omega t}e^{i\mathbf{k}_\parallel\cdot\mathbf{x}_\parallel}\sum_{j=1}^{6}a^{(j)}\sigma_l^{(j)}e^{ik_z^{(j)}z},\quad l=1,2,3\ .\end{aligned} \tag{26}$$

This equation actually defines the coefficients $\sigma_l^{(j)}$, using Eq. (25).

C. Dispersion relations in the superlattice for oblique incidence

We return to the multilayer SL in order to determine the phonon dispersion relation for a general angle of incidence. Each component of $\mathbf{U}$ and $\mathbf{S}$ must satisfy the continuity and periodicity conditions given by Eqs. (4) and (5). This leads to 12 linear equations to be solved for 12 amplitudes $a_A^{(j)}$ and $a_B^{(j)}$ ($j=1,2,\ldots,6$; A and B are the layer index). We define a 6×6 h matrix

$$h(z)=\begin{bmatrix}\varepsilon_l^{(j)}e^{ik_z^{(j)}z}\\ \sigma_l^{(j)}e^{ik_z^{(j)}z}\end{bmatrix},\quad l=1,2,3,\quad j=1,2,\ldots,6 \tag{27}$$

instead of the 2×2 h matrix defined by Eq. (6). Now the 12 linear equations are reduced to the eigenvalue equation of Eq. (8) to be solved for $\chi=e^{iqD}$. Note that M in Eq. (8) is now a 6×6, instead of a 2×2, matrix. By solving this eigenvalue equation, we can obtain the desired phonon dispersion relation for oblique incidence.

Examples of the acoustic-phonon dispersion relation $\nu=\nu(q)$ for two cases of oblique incidence are shown in Fig. 7. These graphs were calculated for the same combination of SL parameters as in Fig. 3(a). These curves do not relate the three modes for the same wave-vector angle, but rather the three with the same value of $\mathbf{k}_\parallel$ in keeping with the discussion above. As expected, intrazone stop bands—gaps in the dispersion relation *within* the folded Brillouin zone—occur at various values of q in addition to the gaps at the zone boundary and zone center. The coupled-mode frequency gaps occur exactly in the regions of the q-ν plane shown schematically in Fig. 5 where the L and ST dispersion curves would otherwise intersect. It is important to note that for phonon propagation in the (110) plane of cubic crystals chosen here, FT phonons are polarized perpendicular to the

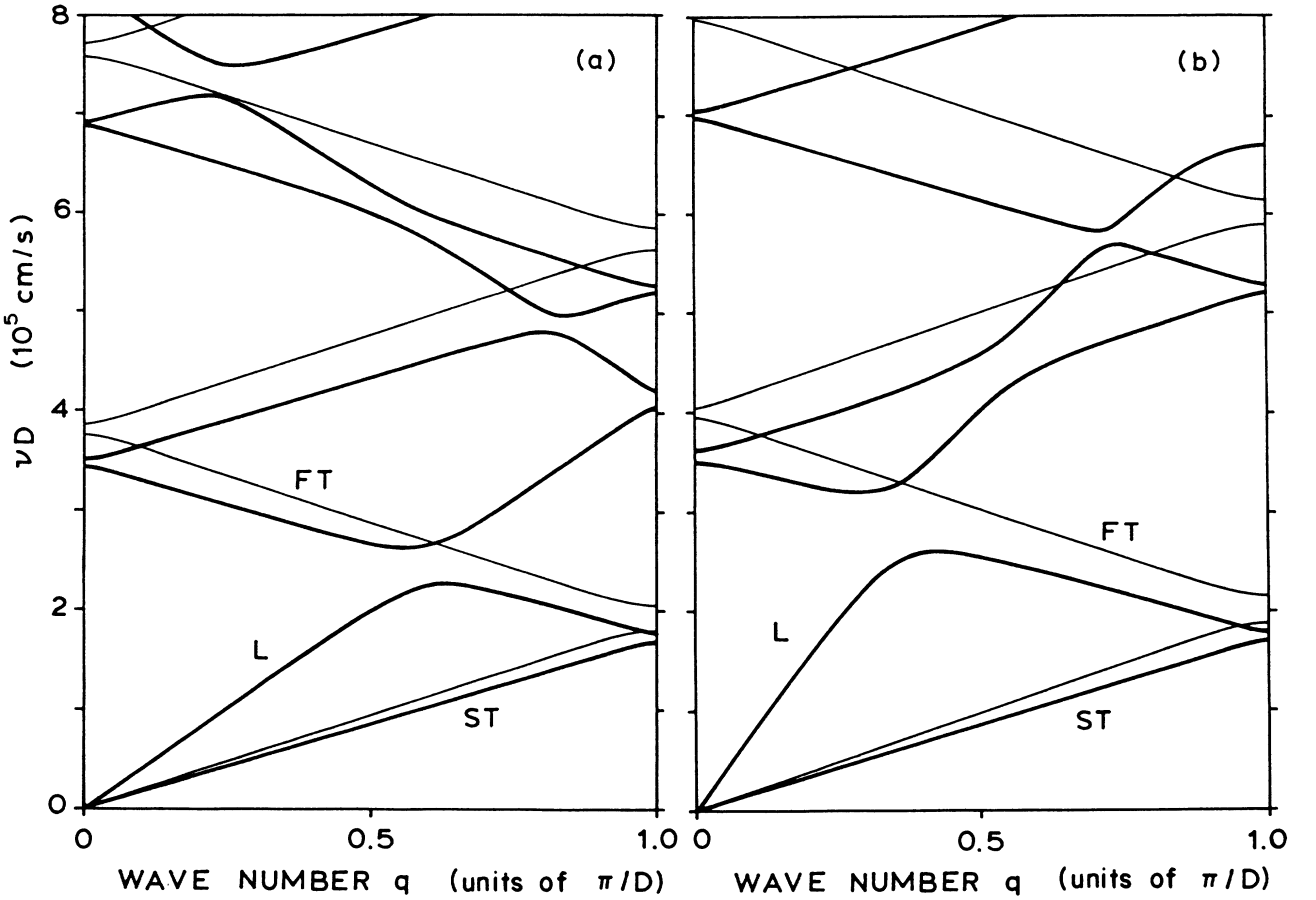

FIG. 7. Normal wave-vector component q vs the product νD for phonons propagating at oblique incidence in an (001) AlAs/GaAs superlattice. (a) Dispersion relation for phonons propagating in the (110) plane, with $\theta_L = 40°$ in GaAs. The corresponding FT and ST angles ($\theta_{FT} = 22.9°$ and $\theta_{ST} = 21.2°$) are determined by conservation of $\mathbf{k}_{\parallel}$. (b) Relation for $\theta_L = 60°$ ($\theta_{FT} = 30.4°$ and $\theta_{ST} = 27.4°$ in GaAs). Intrazone stop bands due to L-ST coupling exist, but for (110) propagation the L and ST modes do not couple with the FT mode, and no L-FT or ST-FT stop bands occur.

(110) plane, and thus they are decoupled from the corresponding ST and L phonons, which are polarized in the plane. Hence in this propagation configuration intermode Bragg reflections do not occur between L and FT or ST and FT phonons, yielding no intrazone frequency gaps in the region where the FT branch intersects the L and ST branches.

We also point out that as the angle of incidence increases, the dispersion curves become steeper, because the wave number q is the z component of the phonon wave vector. This means that the frequency at which stop bands appear becomes larger for a larger angle of incidence. In this respect, it is important to note that, for *a selected experimental frequency,* stop bands originating from different Bragg processes will occur at different angles of incidence.

At low frequencies (where the phonon wavelength is much longer than the SL periodicity) the dispersion curves of three branches are well separated and are quite linear in q. This means that in the SL there is only a very weak coupling between the different polarization modes. Therefore, in the low-frequency region we can write the dispersion relation as

$$\omega = cq \ , \tag{28}$$

where the velocity c is given by

$$c = \frac{Dv_{\parallel}}{\{(d_A\kappa_A)^2 + (d_B\kappa_B)^2 + [(1+\delta^2)/\delta] d_A d_B \kappa_A \kappa_B\}^{1/2}} \ , \tag{29}$$

where $\kappa = k_z/k_{\parallel} = \cot\theta$, and $v_{\parallel} = \omega/k_{\parallel}$, and

$$\delta = \frac{\rho_B \kappa_B \, |\, \mathbf{k}^A \,|^2}{\rho_A \kappa_A \, |\, \mathbf{k}^B \,|^2} \ . \tag{30}$$

The ratio δ in Eq. (30) is the ratio of the effective acoustic impedance for a particular mode in alternating layers [cf. δ in Eq. (9)]. Equation (29) gives the effective phase velocity of the wave along the z axis and reduces to Eq. (11) for normal incidence. Note that these equations also relate q with k_z in each layer at low frequencies. At high frequencies the coupling among different polarizations becomes significant and no such simple analytic expression exists for the dispersion relation.

D. Transmission rates

We next calculate the transmission rate for a single acoustic-phonon mode propagating at oblique incidence through a SL with a finite number of periods [see Fig. 1(b)], allowing for the possibility of mode conversion. In the substrate there are now one $+z$-propagating wave (incident wave) and three $-z$-propagating waves (reflected waves). In the detector layer, only three $+z$-propagating waves (transmitted waves) exist. Within an intermediate SL layer, there are six wave amplitudes.

We again use the column vector $\mathbf{w}$, which now consists of the six wave amplitudes in the nth layer [instead of two amplitudes as in Eq. (12)]:

$$\mathbf{w}_n = \begin{bmatrix} a_n^{(j=1)} \\ \vdots \\ a_n^{(j=6)} \end{bmatrix} . \tag{31}$$

With the 6×6 h matrices defined by Eq. (27), the continuity equations for the displacement and stress vectors at an interface take the same form as Eqs. (13) and (14). Again, we assume that of the six wave amplitudes $a_D^{(j)}$ in the detector layer, the three reflected amplitudes are zero, that is, $a_{2N+1}^{r'(J)} \equiv a_D^{r'(J)} = 0$ for reflected waves in the detector layer, where $J = 1$, 2, and 3 denotes the three phonon modes. Similarly, $a_0^{t'(J)} \equiv a_S^{t'(J)} = \delta_{J,J_0}$ where J_0 represents the mode of incident phonons in the substrate. Thus, Eq. (14) determines the three phonon amplitudes $a_D^{t'(J)}$ transmitted to the detector and the three amplitudes $a_S^{r'(J)}$ reflected in the substrate.

The phonon transmission rate is defined similarly to that in Sec. II, i.e., by the ratio of z components of the energy flux of the transmitted and incident phonons. Here, the velocity V_I in each layer is the z component of the group velocity $\mathbf{V}$ for the relevant mode.

Figures 8(b) and 8(c) show examples of the frequency and layer-thickness dependencies of the transmission rate of the ST and L phonons. The SL parameters and phonon-propagation directions are the same as those in Fig. 7(a), and these dispersion curves are reproduced in Fig. 8(a) for direct identification of the energy gaps with the transmission dips. All of the calculated dips correspond well to the frequency gaps in the dispersion curves. In particular, the dips labeled 1–3 are common to L and ST modes, corresponding to intermode Bragg reflections between L and ST. It is interesting to note that these intermode phonon transmission dips are actually deeper than the dips corresponding to the intramode (zone-boundary) Bragg reflections. This suggests that coupled-mode Bragg reflection of phonons in SL's should be rather easily observed experimentally for oblique propagation configurations.

IV. ANGULAR DISTRIBUTION OF PHONON TRANSMISSION THROUGH A SUPERLATTICE

The transmission rates calculated in Fig. 8 apply only to a *particular* angle of incidence. Yet the anisotropies in the phonon scattering are one of the most interesting features of this system. Of course, many different transmission curves could be generated for successive angles of incidence, but the usable information gained in such a procedure would hardly be worth the effort. Instead, we now consider two alternative procedures for

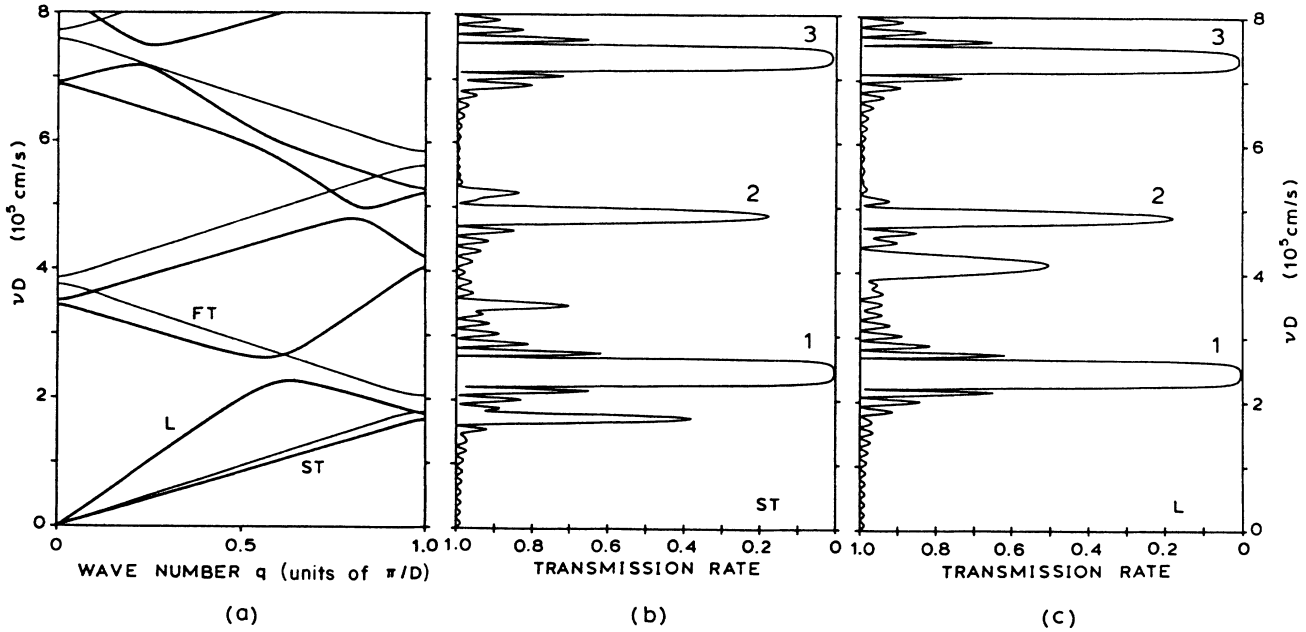

FIG. 8. (a) Dispersion relation for phonons in an (001) AlAs/GaAs SL, as described in Fig. 7(a). (b) Transmission rate vs νD for ST phonons incident on an (001) AlAs/GaAs SL with 15 periods. The propagation direction $\theta_{ST} = 21.2°$ was set to conserve $\mathbf{k}_\parallel$ with the direction for L phonons used in part (c). (c) Transmission vs νD for L-mode phonons in the same SL, $\theta_L = 40°$. In addition to various transmission dips corresponding to the individual zone-edge and zone-center stop bands, both modes share dips labeled 1–3 due to intermode Bragg reflections within the zone.

characterizing the angular dependence of the phonon transmission. The first approach is to plot a two-dimensional spatial map of the Bragg condition for fixed frequencies. Secondly, Monte Carlo techniques are employed to generate the corresponding spatial maps of phonon transmission at a given frequency. The approach is analogous to optical spectroscopy, in which spectral information is transformed to spatial information by the use of a ruled grating. In the phonon case, the SL serves as a "ruled grating." (A closer analogy with the SL is the optical interference filter, which is sometimes used in spectroscopy.)

The utility of such calculations stems from the development of phonon-imaging techniques, whereby the experimenter can easily scan the angle of phonon propagation between the source and detector. (This is generally accomplished by fixing the detector and moving the heat source—an electron or laser beam.) To study SL properties, a phonon-imaging experiment is subject to an additional constraint, namely, a means of frequency selection. This has been accomplished as described in the following section.

Due to the inherent anisotropy of phonon propagation, the SL has a much more complicated response than an optical interference filter. Nevertheless, it is conceivable that future technical developments will permit the SL's use in phonon spectroscopy. In addition to characterizing the physics of acoustic wave propagation through a SL, the present type of calculations provides an essential development towards this end.

A. Spatial maps of the Bragg condition

Using the relation $\lambda = v/\nu$, the usual Bragg condition [Eq. (18)] can be written in the alternate form

$$\frac{\cos\theta}{v} = \frac{m}{2\nu D} . \tag{32}$$

Hence, for a fixed frequency ν in an *isotropic* SL, the mth-order intramode Bragg reflection will occur only for phonons with a single value of the incident angle θ. In a real SL of elastically *anisotropic* materials, v changes with propagation direction, as the slowness surfaces of Fig. 6 indicate. The Bragg angle will vary accordingly depending on the orientation of the saggital plane containing the incident and reflected wave vectors. Therefore, a polar plot of the angles for which Eq. (32) is satisfied provides basic information about the angular dependence of the intramode Bragg reflection. In reality, the situation is a bit more complicated. A phonon-imaging experiment actually scans real space, not **k** space. Thus we must transform the **k** vectors associated with Bragg scattering into the group-velocity vectors of the substrate (GaAs here). The procedure for **k**-to-**V** transformation has been described elsewhere,[17,19] and general computer programs are available to accomplish the task.[20]

The graphs in Fig. 9 show the real-space angles in GaAs that satisfy the Bragg condition for various values of νD, assuming $m = 1$.[21] Also shown (in parentheses) are the corresponding frequencies assuming $D = 40$ Å. In these graphs, the interface normal is the [001] direction, so the angle of incidence is just the polar angle θ. A computer program varied θ for each azimuthal angle ϕ until a pair (θ,ϕ) satisfying Eq. (32) was found. The (θ,ϕ) pairs were then transformed into the real-space angles (Θ,Φ) using the **k**-to-**V** mapping for GaAs. The resulting curves indicate the real-space propagation directions for which the *intra*mode (standard) Bragg reflection attenuates the phonon transmission. The maps in Fig. 9 also contain the patterns of mathematically infinite phonon intensity (caustics) characteristic of phonon focusing, shown as the dashed lines. Figure 9(a) reveals that the L-mode pattern is nearly circular, while the ST and FT patterns in Figs. 9(b) and 9(c), respectively, are more anisotropic when convolved into the focusing structure. Note that increasing the phonon frequency moves the pattern away from the interface normal (i.e., θ increases). These patterns describe a single frequency; for a real stop band, there is a range of attenuated frequencies and the curves have a finite width.

Similarly, substitution of $\lambda = v/\nu$ into the *inter*mode (coupled-mode) Bragg condition [Eq. (19)] yields (e.g., for L↔FT conversion)

$$\left[\frac{\cos\theta_{\rm L}}{v_{\rm L}} + \frac{\cos\theta_{\rm FT}}{v_{\rm FT}}\right] = \frac{m}{\nu D} . \tag{33}$$

For a fixed frequency, conservation of $\mathbf{k}_{\parallel}$ or Snell's law also requires

$$\frac{v_{\rm L}}{\sin\theta_{\rm L}} = \frac{v_{\rm FT}}{\sin\theta_{\rm FT}} = v_{\parallel} . \tag{34}$$

Thus, intermode Bragg reflection occurs for the pairs of angles $(\theta_{\rm L},\theta_{\rm FT})$ that simultaneously satisfy Eqs. (33) and (34) for a given combination of m, ν, and D. Angles for L↔ST and ST↔FT conversion can likewise be determined. Plots of the corresponding real-space angles are shown in Fig. 10. In each case, there are two curves: one for each phonon mode detected, with the appropriate **k**-to-**V** transformation. (In other words, a *particular* L↔T coupled mode stop band is manifested in both the L and T transmission.) The patterns are similar, but not entirely identical to the intramode maps in Fig. 9, indicating the effect of SL anisotropy.

B. Monte Carlo calculations of the stop band distribution

While the simple Bragg-reflection maps described above indicate the basic anisotropies in the reflection process, they do not provide direct information about the strength or angular width of the stop bands. (Note: a range of forbidden frequencies transforms into a range of forbidden angles, so we can equally well use the term "stop band" to describe the real-space attenuation.) To determine the complete spatial distribution of the acoustic stop bands, we present the following method.

An incident **k** vector in the substrate is chosen randomly from a desired input range. A frequency ν is fixed at a single value or selected randomly from the "detector" frequency interval $\nu_1 \le \nu \le \nu_2$. For this **k**, ν, and selected mode J, the value of $\chi = e^{iqD}$ containing the superlattice wave vector q is calculated according to the steps described in Sec. III. If $|\chi|^2 = 1$, then q is a real

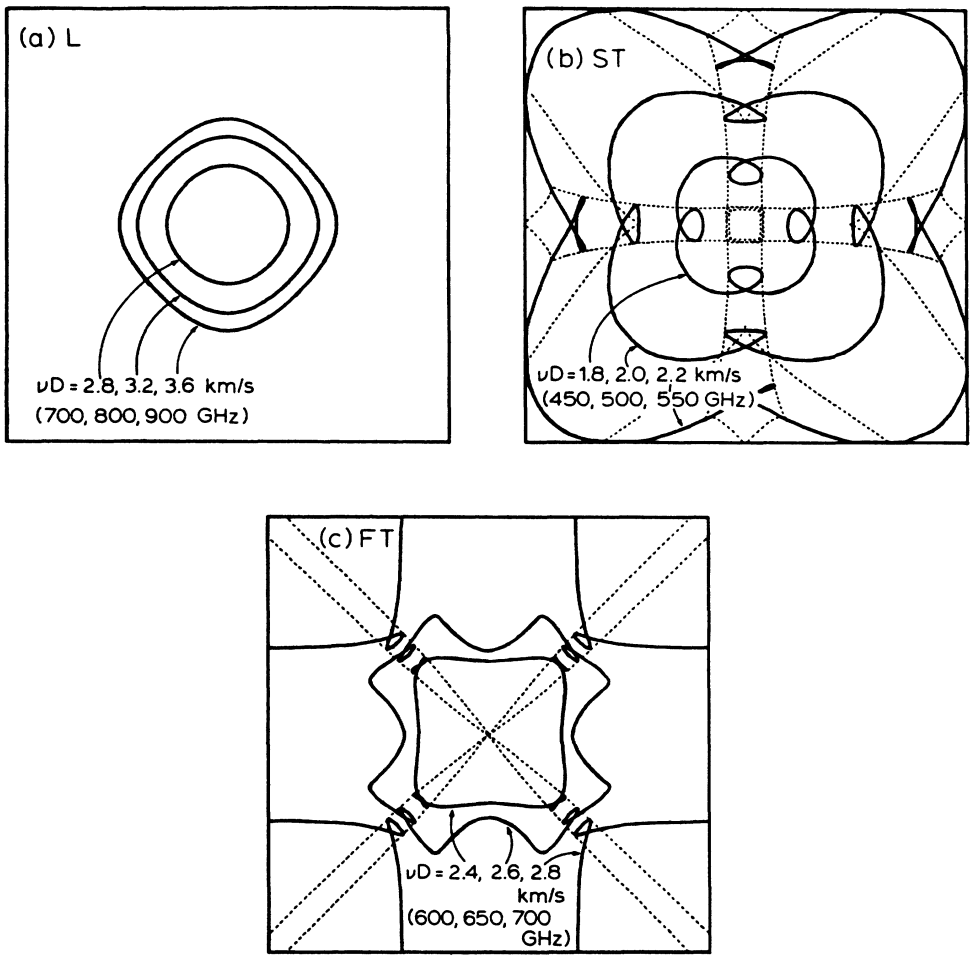

FIG. 9. Spatial maps of the intramode Bragg condition for phonons incident on an (001) AlAs/GaAs SL from a GaAs substrate. These maps show the set of real-space directions for which Eq. (32) in the text is satisfied. The maps span $\pm 63°$ ($\tan\Theta = \pm 2$). The dashed lines in parts (b) and (c) indicate the phonon-focusing caustics for FT and ST phonons in GaAs. (a) Curves for L phonons with $\nu D = 2.8$, 3.2, and 3.6 km/s. For a SL with $D = 40$ Å, the curves represent $m = 1$ Bragg reflection of L phonons with $\nu = 700$, 800, and 900 GHz, respectively. (b) Map for FT phonons with $\nu D = 2.4$, 2.6, and 2.8 km/s ($m = 1$ reflection for phonons with $\nu = 600$, 650, and 700 GHz). (c) Map for ST phonons with $\nu D = 1.8$, 2.0, and 2.2 km/s ($m = 1$ reflections for $\nu = 450$, 500, and 550 GHz).

wave vector and can propagate through the SL. If $|\chi|^2 \neq 1$, then q is an imaginary wave vector (i.e., it lies in a stop band). The real-space direction of these imaginary wave vectors are computed, and projected onto the desired viewing plane. Thus the dark areas in the finished two-dimensional plot mark the positions of acoustic stop bands, and the local density of points correspond to the flux of initial **k** vectors intersecting that region. Thus, the dark areas represent the distribution of *reflected* phonons. The crystalline symmetry (fourfold here) is exploited to yield better statistics. Typically, a calculation requires 15 000 incident **k** vectors, which results in 9000 stop-band points and takes 100 min of CPU time on a VAX 750 computer.

Such Monte Carlo calculations of the stop-band distribution are shown in Fig. 11. The figure shows stop-band distributions for each of the three phonon modes in an AlAs/GaAs SL with $d_A = d_B = D/2 = 20$ Å. The assumed frequencies are 700, 600, and 500 GHz for L, FT, and ST phonons, respectively. In each case a very narrow band of frequencies is sampled ($\Delta\nu = 10$ GHz). In these figures one can recognize stop-band distributions similar to the contour maps in Figs. 9 and 10. However, some of these features are quite broad, because the finite width of the frequency gaps produces a finite spatial range of stop bands for a single frequency. Moreover, the calculations reinforce our prediction of stop-band structures due to both intra- and intermode Bragg reflections in this frequency range. The outermost structures are not due to Bragg reflections at all, but instead are due to waves in the "harder" AlAs layer that become evanescent, localized near the interfaces. It should be noted

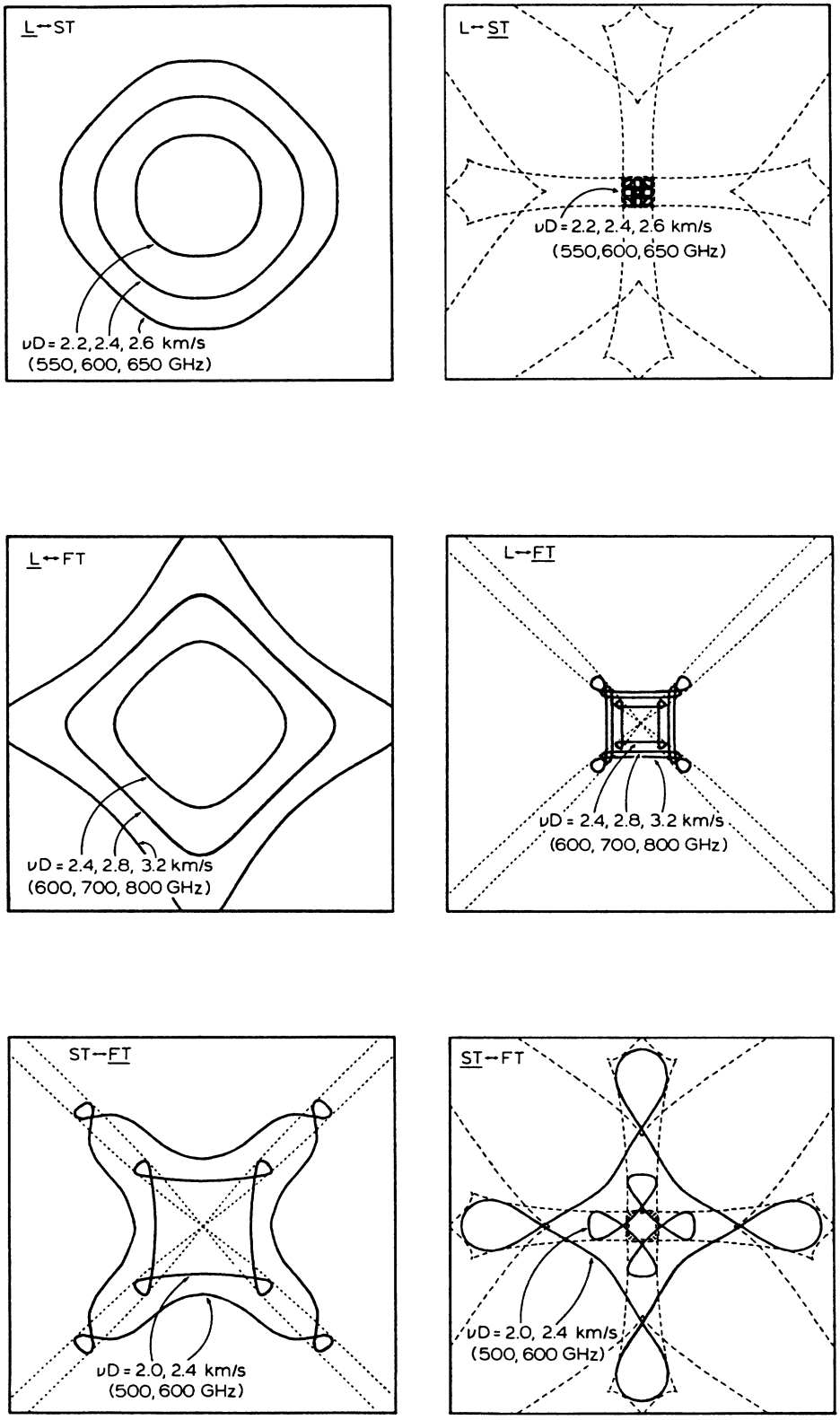

FIG. 10. Spatial maps of the intermode Bragg condition for phonons incident on a (001) AlAs/GaAs SL from a GaAs substrate. Each pair of maps shows the real-space angles for both modes which simultaneously satisfy Eqs. (33) and (34) in the text. The scale of the maps is $\pm 63°$ ($\tan\Theta = \pm 2$). The dashed lines show the FT and ST phonon-focusing caustics for GaAs. (a) Curves for L↔FT mode conversion with $\nu D = 2.4$, 2.8, and 3.2 km/s. For $m = 1$ reflections in a SL with $D = 40$ Å, this corresponds to $\nu = 600$, 700, and 800 GHz, respectively. (b) Map for L↔ST coupling, with $\nu D = 2.2$, 2.4, and 2.6 km/s ($\nu = 550$, 600, and 650 GHz, respectively, for the SL described above). The ST curves all appear within 10° of the [001] direction. (c) Curves for FT↔ST conversion with $\nu D = 2.0$ and 2.4 km/s ($\nu = 500$ and 600 GHz, respectively, in the same SL system).

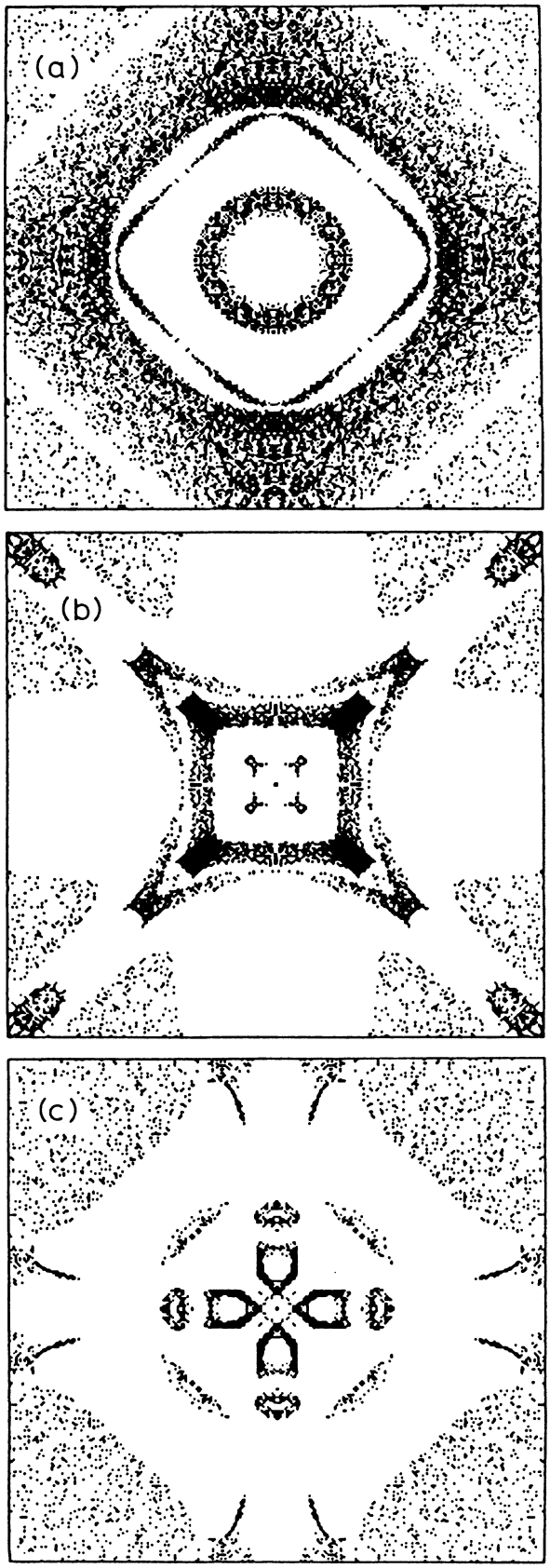

FIG. 11. Monte Carlo calculations of the spatial distribution of phonon stop bands in a (001) AlAs/GaAs superlattice, $D=40$ Å ($d_A=d_B=20$ Å). The images span ±63°. (a) L mode (700 GHz). (b) FT mode (600 GHz). (c) ST mode (500 GHz).

that all of the stop-band structures are very sensitive to the phonon mode and frequency, as well as the SL constituents and their thicknesses.

V. COMPARISON WITH PHONON-IMAGING EXPERIMENTS

The phonon-imaging technique is an ideal experimental means of measuring the angular (spatial) distribution of the acoustic stop bands in superlattices. Phonon imaging provides a two-dimensional map of the intensity variation for each mode as a function of propagation direction. Individual modes can be isolated by velocity selection. Such experimental results can be directly compared to the theoretical results discussed above.

The phonon-imaging technique used here is based upon that developed by Northrup and Wolfe.[22] The samples involved were high-quality AlAs/GaAs and $In_xGa_{1-x}As$/AlAs heterostructures grown by the molecular-beam-epitaxy (MBE) technique on commercial undoped GaAs wafers ($\sim$400 μm thick).[23] A 2000-Å-thick Cu film was deposited on the face of the substrate opposite the SL. The sample is immersed in liquid He ($T\approx 1.8$ K). A pulsed Ar^+ laser beam ($\lambda=5145$ Å, width ≈ 15 ns, spot-size diameter ≈ 10 μm) is raster-scanned across the metalized surface, thereby exciting electrons in the Cu film. Phonons created by the relaxation of the electrons propagate across the substrate, through the SL, and are detected by a (15×15)-μm^2 PbBi tunnel junction. A boxcar integrator affords temporal resolution of the detected intensity signal, so that the polarization modes may be distinguished by their differing times of flight. Generally, the boxcar gate is continuously adjusted during the X-Y scan in order to select a constant velocity as the path length between the source and detector changes. The transmitted phonon intensity is recorded as the boxcar output voltage for a particular laser-spot position. A (256×256)-element array is digitally recorded and displayed on a video monitor using a video-frame buffer.

The Pb-Bi tunnel junction is an extremely useful and versatile phonon detector.[24] A tunnel junction detects phonons with energy $h\nu \geq 2\Delta$, where 2Δ is the superconducting gap. This detection onset is an important factor in the experimental frequency resolution. The stoichiometry of the Pb-Bi alloy may be altered to obtain a particular phonon onset frequency ν_c in the range $650 \leq \nu_c < 850$ GHz.[25] The onset frequency of an individual detector is determined from its I-V characteristics. Figure 12(a) shows the I-V characteristics of one of the detectors we used. The onset frequency ν_c equals $2\Delta/h$. Moreover, the substrate acts as a low-pass filter which in conjunction with the detector onset provides a band of detected frequencies, $\Delta\nu_D \sim 0.2\nu_c$. Isotope scattering in the bulk crystal and scattering from impurities and defects contribute to this high-frequency cutoff. Theoretical and experimental discussions of this useful frequency-selectivity effect have been published for GaAs and InSb.[26–29]

To illustrate the frequency-selectivity effect, Fig. 12 shows the predicted transmitted phonon distribution for

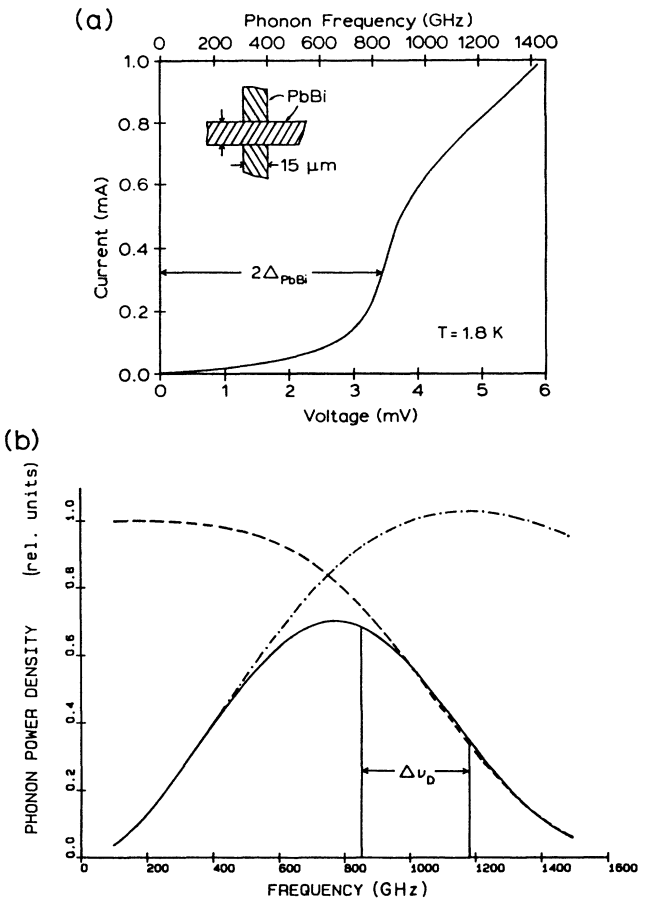

FIG. 12. (a) I-V characteristics of Pb-Bi tunnel junction. (b) Predicted frequency distribution for L phonons in a 400-μm-thick GaAs crystal when isotope scattering effects are included. The dashed-dotted line indicates a 20-K Planck phonon distribution. The dashed line represents the transmission factor $e^{-D/V\tau}$ calculated with the isotope scattering rate in Ref. 26 and a single phonon velocity $V=5.4$ km/s. The solid line is the transmitted distribution, Planck$\times e^{-D/V\tau}$. The phonon frequency range for a detector with onset frequency 850 GHz is indicated by $\Delta\nu_D$, assuming only isotope scattering.

L phonons in a 400-μm-thick GaAs crystal, assuming only defect scattering from isotopes. The dashed-dotted line represents an initial 20-K Planck phonon distribution. The dashed line depicts the attenuation due to isotope scattering calculated from theoretical estimates for GaAs.[26] The detected frequency band $\Delta\nu_D$ is defined as the full width at half maximum (FWHM) of the detected distribution. As indicated in the figure, for a detector with $\nu_c=850$ GHz, $\Delta\nu_D\approx 350$ GHz. This transmitted phonon frequency is somewhat larger than what we estimate from the SL results to be described, indicating that defects in the substrate other than isotopes are limiting the high-ν transmission.

Experimental phonon images for the GaAs substrate are shown in Fig. 13. Figure 13(a) is constant-velocity image of the L-phonon intensity ($v=5.4$ km/s, $\nu_c\approx 850$ GHz). For all of the experimental images, the center of the image is ⟨001⟩, and ⟨111⟩ directions are located approximately at the positions indicated by crosses in Fig. 13(a). The regions of relatively high intensity stretching between adjacent ⟨111⟩ directions are an expected consequence of phonon focusing. The image displays a higher intensity in the vicinity of ⟨001⟩ (center of image) than expected from phonon focusing. We attribute this extra intensity to L phonons that undergo small-angle scattering in the substrate. The scattering could be due to isotopes or defects in the substrate. Figure 13(b) shows a phonon image for the same GaAs sample, selecting a longer time of flight (230 ns). The relatively broad boxcar gate (80 ns) makes it possible to detect most of the FT and ST patterns over a wide range of angles. At these frequencies, dispersion causes a noticeable increase in the angular separation of the FT caustics, and a rounding of the central ST structure.[26,27,30]

With the phonon images for the GaAs substrate in mind, the imaging experiments were repeated for several substrate-plus-SL samples. (Unless otherwise indicated,

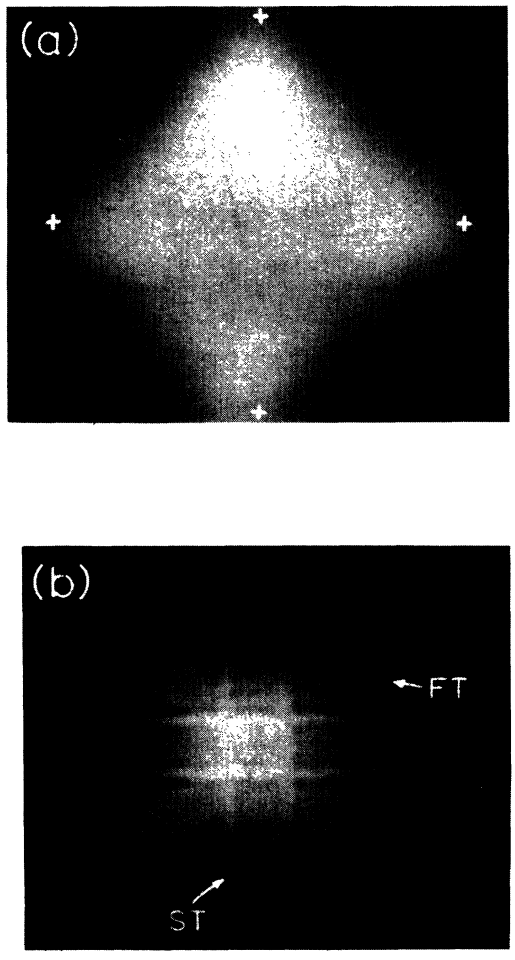

FIG. 13. Experimental phonon images of the phonon flux intensity in an (001)-oriented GaAs substrate. (a) Constant-velocity image of L phonons ($v=5.4$ km/s). The image is centered on the [100] direction, and spans approximately ±60° left to right. Adjacent ⟨111⟩ directions are indicated by the crosses. (b) Constant-delay image (gate 80 ns wide at $t=230$ ns after the laser pulse) of FT- and ST-phonon intensities. The bright lines of high flux intensity (caustics) are due to phonon focusing. A 25-μm Gaussian broadening due to finite laser-spot and detector resolution has been deconvolved from this image.

all detectors were fabricated to obtain a phonon onset frequency $\nu_c \approx 850$ GHz.) For the first experiment, the tunnel junction was evaporated directly over an $In_{0.15}Ga_{0.85}As/AlAs$ SL with $d_A = d_B = 20$ Å and 40 periods. Figure 14(a) is a constant-velocity image for the L phonons. The most striking feature is the narrow, nearly circular "dip" in the phonon transmission. Figure 14(b) shows the phonon intensity for a scan line across the center of the image. The dashed line in this figure represents a similar scan across the center of the substrate sample in Fig. 13(a). (The substrate intensity is plotted above that of the SL sample. Since the two experiments involved different detectors with different characteristics, the relative intensities of the two samples can only be estimated.) Note that the transmission dip is quite sharp, indicating a relatively narrow range of detected frequencies. The total effect of the SL may be better isolated by subtracting the substrate image in Fig. 13(a) from the substrate-plus-SL image in Fig. 14(a). This *difference* image, which roughly represents the SL attenuation, is shown in Fig. 14(c) with increased gain. In addition to the sharp ring, a diamond-shaped structure is apparent. We now address the origin of these SL effects.

A Monte Carlo calculation of the L stop bands for $\nu = 845-855$ GHz in this SL is shown in Fig. 14(d). As in Fig. 11, a dot indicates the direction of the phonon group velocity projected onto the (001) plane of the GaAs substrate. Three different stop-band structures are apparent in this figure: narrow circular and diamond-shaped structures, and a broad distribution surrounding them. This simulation is quite similar to the experimental observations. The ring corresponds to the $m = 1$ zone-boundary stop band [Δ_L in Fig. 15(a)] and experimentally occurs at $\Theta = 35° \pm 3°$ from $\langle 001 \rangle$ in the (100) plane and $\Theta = 37° \pm 3°$ in the (110) plane. Figure 14(d) predicts $\Theta = 38.7° \pm 0.8°$ for (100) and $\Theta = 40.6° \pm 0.6°$ for (110). A 2-Å uncertainty in the layer thickness, or the use of non-dispersive elasticity theory, could account for the small

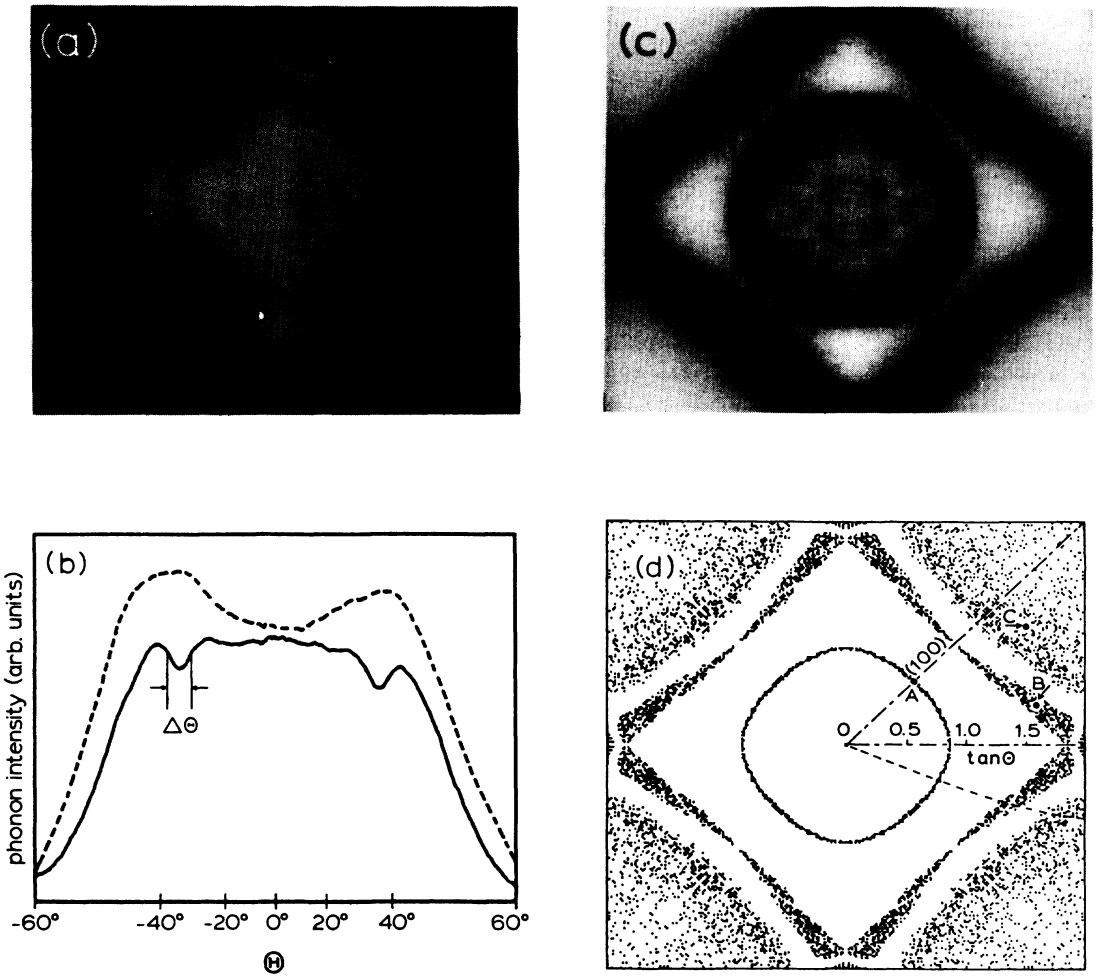

FIG. 14. Phonon images for a (001) $In_{0.15}Ga_{0.85}As/AlAs$ SL with $d_A = d_B = D/2 = 20$ Å and 40 periods. (a) Experimental constant-velocity image of L phonons ($v = 5.4$ km/s). The image scale and orientation are approximately the same as in Fig. 13(a). (b) Scan of phonon intensity across the center of the image for the SL sample (solid line) and the substrate sample (dashed line). The relative intensities of the two curves is arbitrary for display purposes. (c) Difference image created by subtracting the substrate image of Fig. 13(a) from the SL-plus-substrate image in (a), shown at increased gain. To improve the signal-to-noise ratio, the four symmetry-related quadrants have been averaged. (d) Calculated stop-band distribution for L phonons in this system. The dashed line and points A, B, and C are for reference in Figs. 15 and 16.

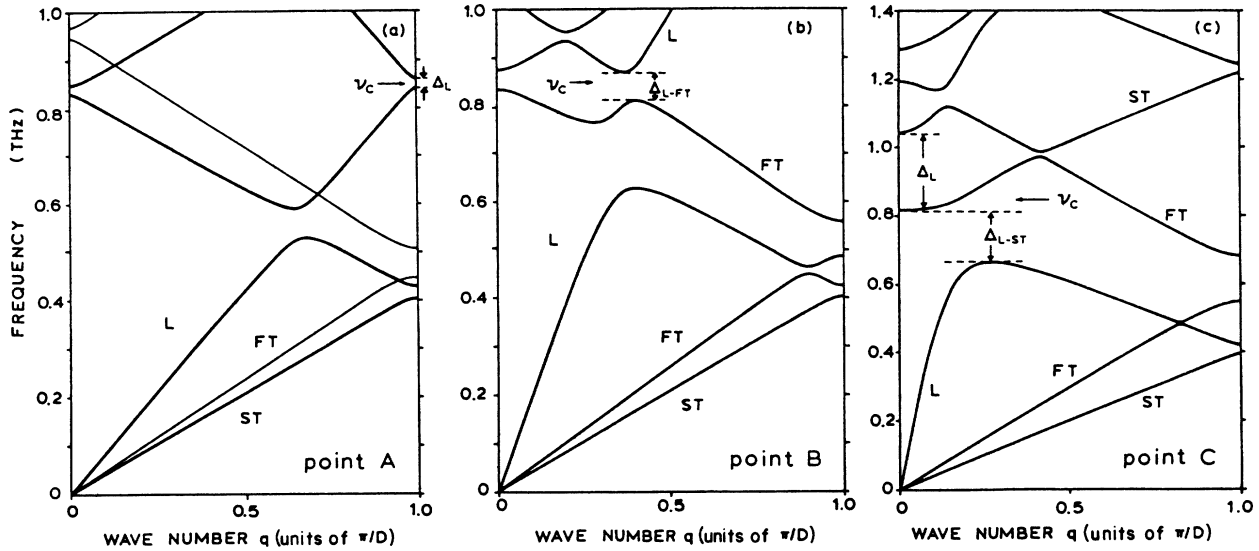

FIG. 15. (a) Phonon dispersion relation for the propagation direction indicated by point A in Fig. 14(d). (b) Dispersion relation for the propagation direction indicated by point B in Fig. 14(d). (c) Relation for the propagation direction indicated by point C in Fig. 14(d). Note that the frequency scale in (c) has been changed. As the phonon angle of incidence is increased, the curves grow steeper. Thus for a fixed detector frequency (lower limit or onset frequency of 850 GHz indicated by ν_c), it is possible to detect different types of stop bands by varying the phonon angle of incidence.

discrepancy between theory and experiment.

In order to identify the origins of the stop-band structures, we have calculated the dispersion relations for L phonons propagating in the three different directions A, B, and C indicated in Fig. 14(d). The results, shown in Figs. 15(a)–15(c), indicate band gaps for the L phonons which coincide with $\nu=\nu_c=850$ GHz. The gap appearing for propagation along A is the lowest ($m=1$) zone-boundary stop band, Δ_L. For propagation along B, an intrazone frequency gap $\Delta_{L\text{-}FT}$ due to coupling of the L and FT modes coincides with the detector onset frequency. For propagation along direction C, the dispersion relation is more complicated. At this large angle of incidence, the L dispersion curve is very steep, and a stop band due to L-ST coupling occurs close to $q=0$. As a result, the coupled-mode gap $\Delta_{L\text{-}ST}$ and the zone-center gap Δ_L appear continuously in frequency. In Fig. 15(c), $\nu=\nu_c=850$ GHz falls within the zone-center gap Δ_L rather than in the gap $\Delta_{L\text{-}ST}$. However, at slightly larger angles of incidence, $\nu=\nu_c$ falls within $\Delta_{L\text{-}ST}$. Thus, the theoretical image in Fig. 14(d) contains all possible types of L stop-band structures originating from inter- and intramode Bragg reflection of L phonons in the SL.

To compare with the experimental images, Fig. 16(a) shows the calculated transmission rate of L phonons along the dashed line of Fig. 14(d). The frequency is again fixed at 850 GHz, and 20 SL periods were used for the calculation. [The dashed line in Fig. 14(d) is curved because the azimuthal angle ϕ is fixed at $\phi=19°$.] Very sharp dips in the transmission are obtained for angles where the first-order intramode Bragg reflection and the L-FT intermode Bragg reflection occur. However, the reduction in transmission is relatively small for the angles corresponding to the outermost stop-band structure. In addition, the phonon intensity at these large angles is small by geometrical arguments. Thus, Fig. 16(a) helps to explain why the broad outermost stop-band distributions are not experimentally observed, while the two innermost structures are.

Figure 16(b) shows a corresponding plot for the experimental data. The curve represents the transmitted phonon intensity for the image in Fig. 14(a) along a straight line $\Phi=20°$, divided by the corresponding curve for the substrate in Fig. 13(a) ("normalized phonon intensity"). The angular positions of the dips in experimental flux agree reasonably well with the calculations, but the experimental dips are broader. This could be due to SL imperfections and a nonmonochromatic phonon source. To simulate the effect of a nonmonochromatic source, Fig. 17 shows the stop-band distribution for L phonons in the $In_{0.15}Ga_{0.85}As/AlAs$ superlattice described above, assuming a range of frequencies $\nu=850$–950 GHz. For this wider frequency range, the ring structure due to the zone-boundary stop band is considerably broader, and the outer L-ST and L-FT structures are merged together into one broad structure. However, the coupled-mode structure is still quite anisotropic and is well separated from the zone-boundary feature.

We can more quantitatively estimate the effects of a finite-frequency distribution. The width of the $m=1$ transmission dip is an indication of the detected frequency range $\Delta\nu_D$; i.e., the spatial position of the dip changes with frequency, and so the dip width is proportional to $\Delta\nu_D$. The FWHM of the dip, $\Delta\Theta$ [indicated in Fig. 14(b)], is approximately 6°. When compared with calculations of the phonon transmission as a function of angle for a discrete range of frequencies, this $\Delta\Theta$ implies $\Delta\nu_D\approx150$ GHz. In addition, $\Delta\nu_D$ can be estimated for

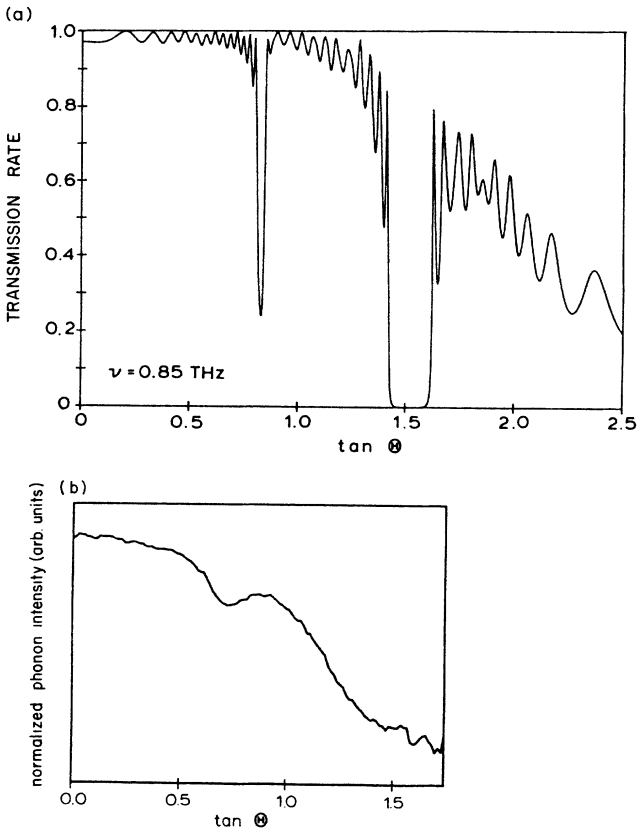

FIG. 16. (a) Calculated transmission rate of L phonons ($\nu=850$ GHz) as a function of angle Θ in an $In_{0.15}Ga_{0.85}As/AlAs$ SL with 20 periods ($d_A=d_B=20$ Å). The propagation directions correspond to those along the dashed line in Fig. 14(d), in which ϕ is fixed at 19° (Φ is varied with Θ). (b) Experimental phonon intensity for a line $\Phi=20°$, divided by the same intensity in the substrate sample.

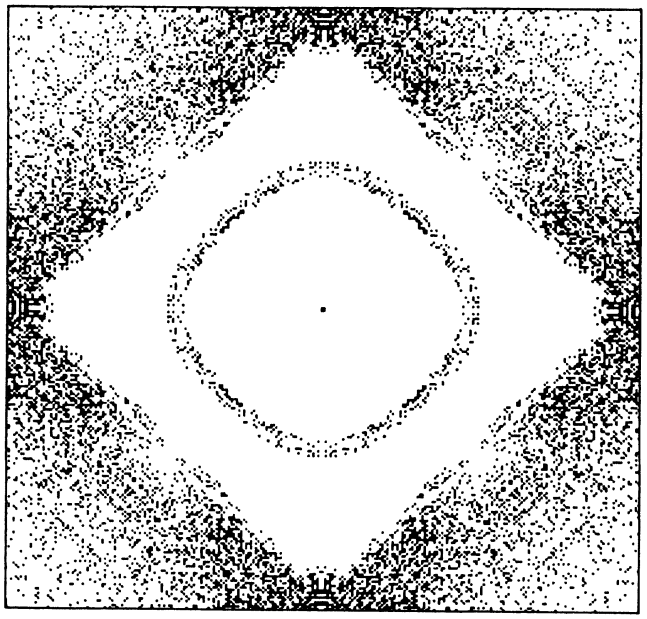

FIG. 17. Calculated stop-band distribution identical to that in Fig. 14(d), except that an input frequency range $\nu=850$–950 GHz has been used. The stop-band features have broadened, but are still distinct.

the transverse phonons as well. Because the FT intensity pattern is quite sensitive to dispersion, the width of the caustics is indicative of the frequency range present. Therefore, the FWHM of the FT caustics at $\Theta=45°$ was measured and compared to the corresponding theoretical prediction, which was calculated using a lattice-dynamics model including both dispersive and isotope scattering effects.[26] The theoretical values indicate that the experimentally measured FWHM corresponds to a frequency range $\nu=850$–1050 GHz. Both measurements support our belief that the GaAs substrate is inhibiting the transmission of ballistic phonons with $\nu \gtrsim 1$ THz. Moreover, Fig. 12(b) indicates that isotope scattering alone is not sufficient to produce such a narrow $\Delta\nu_D$. A scattering rate of 2–3 times that caused by naturally occurring isotopes, most likely due to impurities and other defects, is necessary to understand the sharpness of the SL dip.

A phonon image for L-mode phonons in an $In_{0.25}Ga_{0.75}As/AlAs$ SL with the same layer parameters is shown in Fig. 18(a). The change in material composition has little effect on the transmission attenuation. The intensity line scan in Fig. 18(b) indicates that the $m=1$ stop-band effect is quite similar to that for the previous SL. A difference image is shown in Fig. 18(c), and the predicted stop-band distribution for $\nu=850$–950 GHz is shown in Fig. 18(d). We believe that the intensity differences between Figs. 14 and 18, especially in the subtracted images, can be due to slight differences in the selected phonon velocity and signal gain.

Phonon-imaging experiments were also performed on two additional SL samples consisting of AlAs/GaAs layers. Figures 19(a) and 19(c) show the constant-velocity image and the difference image, respectively, for L-phonon transmission in an AlAs/GaAs SL with $d_A=d_B=20$ Å and 20 periods. Figure 19(b) shows the intensity for a line across the center of the image (solid line), compared to the similar substrate intensity (dashed line). As the line scan and difference image especially reveal, there are indeed some SL attenuation effects. In particular, the scattered phonon intensity near $\langle 001 \rangle$ is noticeably reduced and rather sharply delineated, and the wide-angle intensity falls off slightly faster than for the substrate alone. The theoretical calculation of the spatial stop-band distribution, Fig. 19(d), indicates that such an effect is due to coupled-mode stop-band structures such as those in the $In_xGa_{1-x}As/AlAs$ samples. However, most of the attenuation structures in Fig. 19(c) do not resemble their counterparts in Fig. 19(d). It is possible that the SL layers are not precisely the thickness quoted above (values obtained from growth-rate estimates). On this length scale, even a monolayer of material (2–3 Å) is a sizable fraction of the total thickness.

Phonon-imaging results for a similar AlAs/GaAs SL with $d_A=d_B=15$ Å (40 periods) are shown in Figs. 20(a)–20(c). A layer-thickness designation of 15 Å is somewhat questionable, because it does not nominally

correspond to a commensurate number of lattice spacings. The quoted layer thickness, 15 Å, is simply the average thickness derived from the growth rate. The attenuation pattern is quite similar to that in Fig. 19(c), except that the central region of attenuation is not as sharply defined. For comparison with this experimental image, we have generated theoretical stop-band distributions for $d_A = d_B = 14$ Å (corresponding to five atomic monolayers) and for $d_A = d_B = 17$ Å (corresponding to six atomic monolayers), shown in Figs. 20(d) and 20(e), respectively. These two calculations show the sensitivity of the stop bands to a change in thickness of a single atomic layer. Microscopic information about the actual SL structure is needed in order to generate an appropriate theoretical model. It seems significant, however, that definite stop-band effects are observed for these growing conditions.

We also observe attenuation of transverse phonons in these experiments. Figure 21 shows a fixed-delay image of the FT- and ST-phonon intensities in the $In_{0.15}Ga_{0.85}As/AlAs$ SL mentioned above. Here, the detector cut-in frequency is $\nu_c = 700$ GHz. Comparison with the substrate image in Fig. 13(b) reveals an interesting effect due to the SL. Both a dip in the transmission and a slight shift in the positions of the FT-phonon–focusing caustics are apparent. The theoretical calculations in Fig. 22 help to explain this effect. Figure 22(a) shows the predicted FT stop bands for $\nu = 700$ GHz. For 900-GHz phonons, the FT zone-boundary stop band (Δ_{FT}) shifts further away from $\langle 001 \rangle$, as indicated in

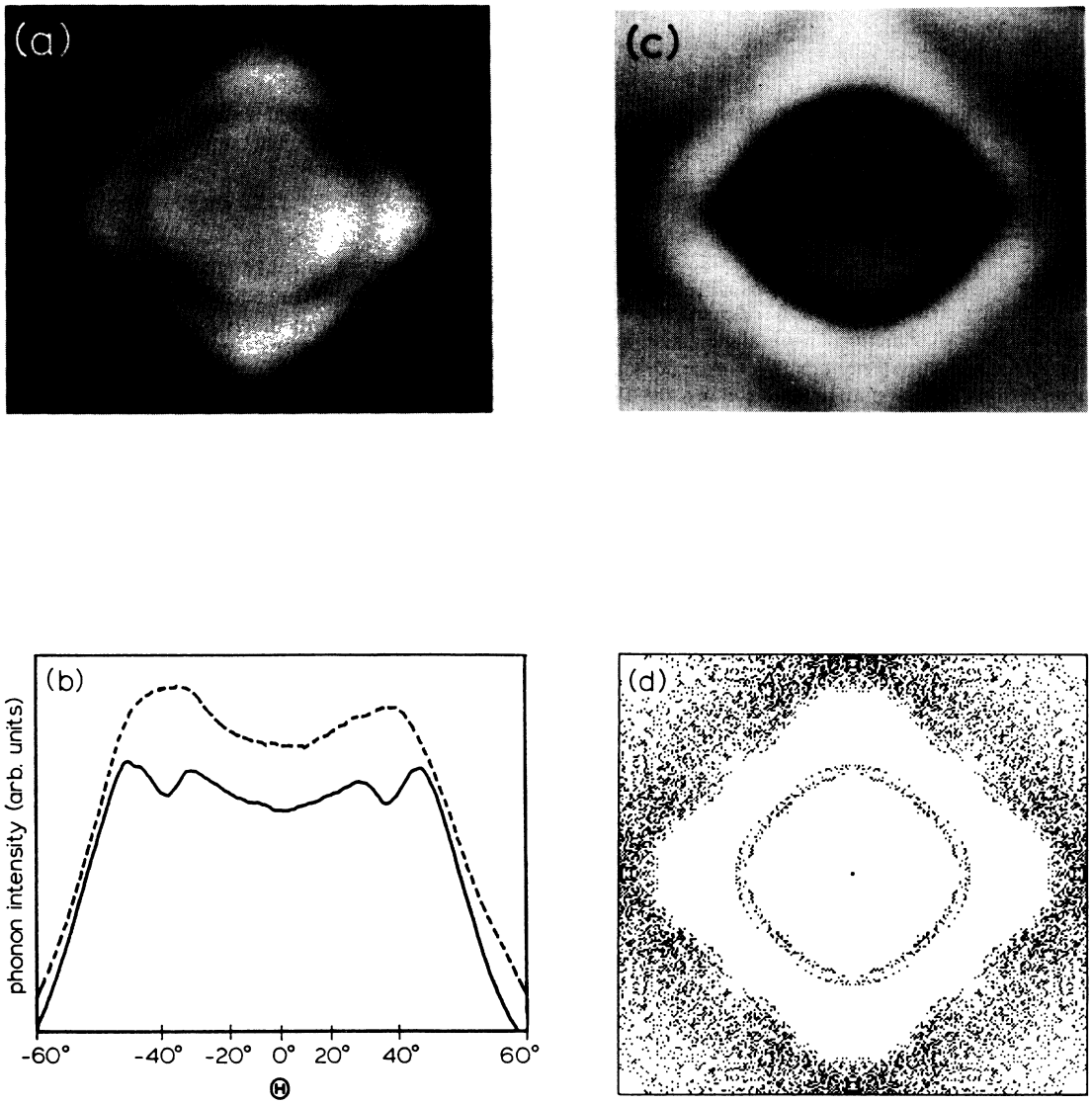

FIG. 18. Phonon images for a (001) $In_{0.25}Ga_{0.75}As/AlAs$ SL with $d_A = d_B = 20$ Å and 40 periods. (a) Experimental constant-velocity phonon image of L phonons ($v = 5.4$ km/s). The image scale and orientation are the same as in Fig. 13(a). (b) Intensity scan across central line in image in (a) (solid line) and substrate sample (dashed line). (c) Difference image, shown with the same amplification as the image in Fig. 14(c). (d) Calculated image of L-mode stop-band distribution for $\nu = 850$–950 GHz.

Fig. 22(b). However, caustics for 700- and 900-GHz phonons are separated due to dispersion, as shown in Fig. 22(c). Combining these effects, we show schematically in Fig. 22(d) the expected intensity pattern for a *distribution* of frequencies between 700 and 900 GHz. All phonons in this frequency range display a small common gap of reduced transmission. This gap and the apparent shifting of the caustics are precisely what is observed in the experimental image of Fig. 21.

Attenuation of FT phonons is also observed in the AlAs/GaAs system. Figure 23(a) indicates the predicted stop-band distribution for $\nu=(850-900)$-GHz FT phonons in an AlAs/GaAs SL ($d_A=d_B=20$ Å). As for the $In_{0.15}Ga_{0.85}As$/AlAs SL, an $m=1$ intramode Bragg reflection is predicted at these frequencies. However, the stop bands are difficult to discern in experimental images for the following reason. For $\nu \gtrsim 850$ GHz, the phonon mean free path is smaller than the path length for large incident angles; high-frequency phonons are scattered and the large-angle intensity is even smaller than indicated by normal geometrical effects. Combination of this effect with the intensity gap due to a stop band produces in the experimental image a sudden falloff of the FT-phonon intensity. This intensity cutoff, indicative of a stop-band onset, is easier to detect by plotting the intensity along a FT caustic, indicated by the solid line in Fig. 23(a). Figure 23(b) shows the FT caustic intensity for the SL sample (solid line) as well as the substrate (dashed line). A normalized transmission is obtained by dividing the SL curve by the substrate curve. This "normalized phonon intensity," represented in Fig. 23(c), clearly indicates a FT cutoff. The onset of the stop band may be estimated to be at the point where the intensity drops by a factor of 2. This occurs experimentally at $\Theta=43°\pm2°$ and

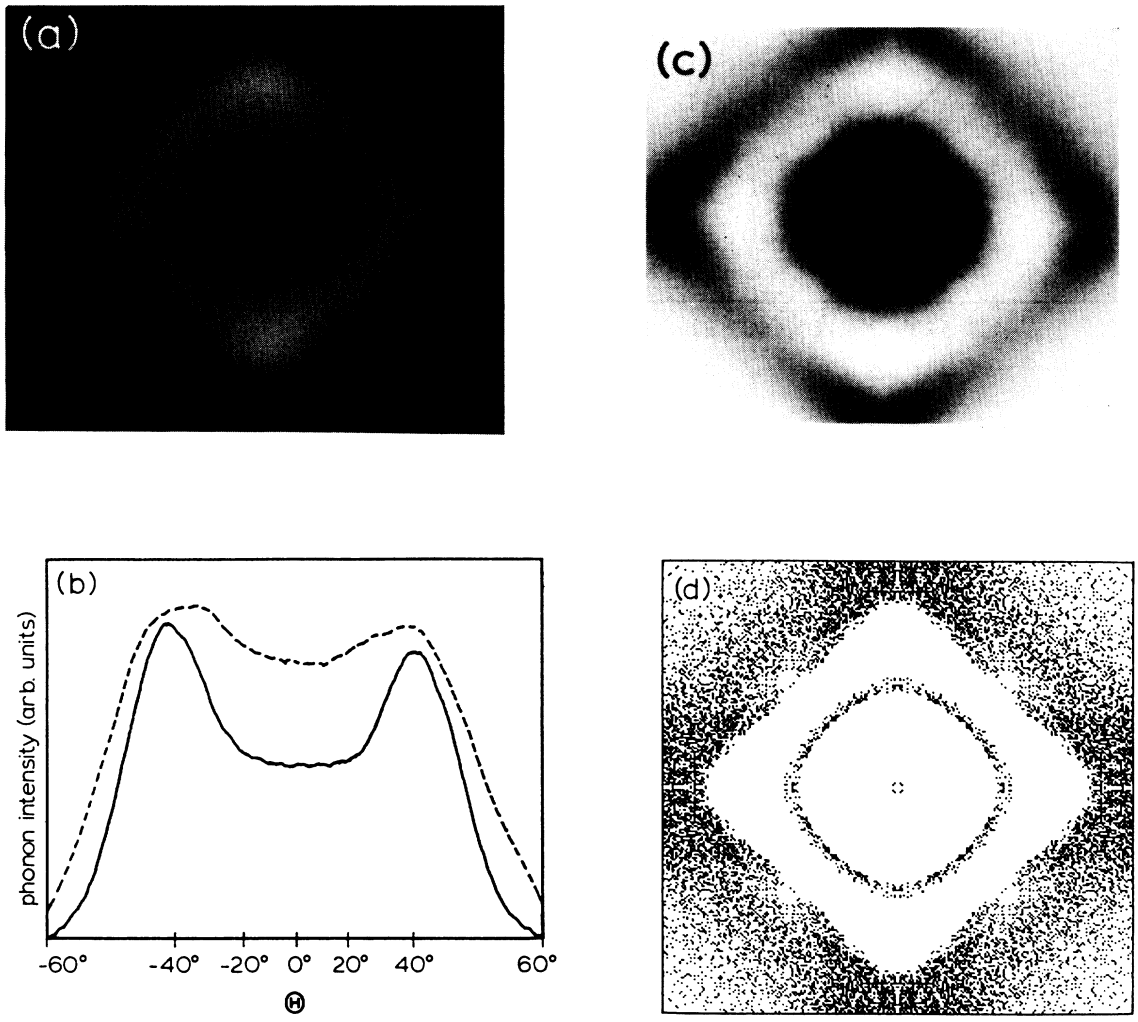

FIG. 19. Experiment and theory for L phonons in an AlAs/GaAs SL with $d_A=d_B=20$ Å and 20 periods. (a) Experimental constant-velocity phonon image ($v=5.4$ km/s). Image scale and orientation are approximately the same as in Fig. 13(a). (b) Intensity across scan line in center of (a) (solid line) and substrate (dashed line). (c) Difference image. (d) Theoretically predicted stop-band distribution for L phonons, $\nu=850-950$ GHz.

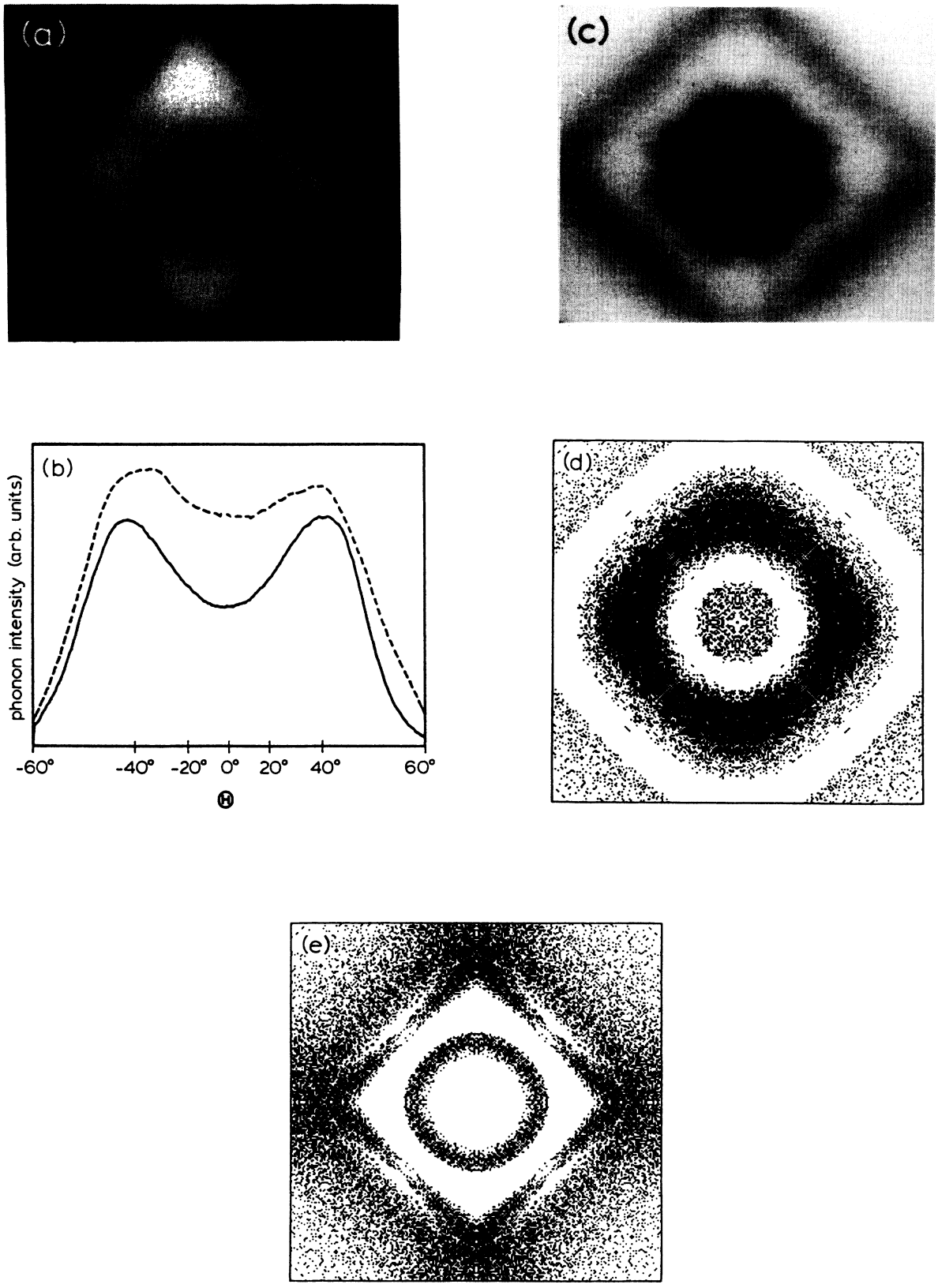

FIG. 20. (a) Experimental constant-velocity image ($v = 5.4$ km/s) for L phonons in an AlAs/GaAs SL with $d_A = d_B = 15$ Å and 40 periods. The image scale and orientation are the same as in Fig. 13(a). (b) Intensity vs position for line across center of (a) (solid line) and substrate sample (dashed line). (c) Difference image. (d) Calculated spatial stop-band distribution ($\nu = 850$–950 GHz) for an AlAs/GaAs SL with $d_A = d_B = 14$ Å, corresponding to five atomic monolayers. (e) Predicted distribution of L-mode stop bands for an AlAs/GaAs SL with $d_A = d_B = 17$ Å, corresponding to six atomic monolayers.

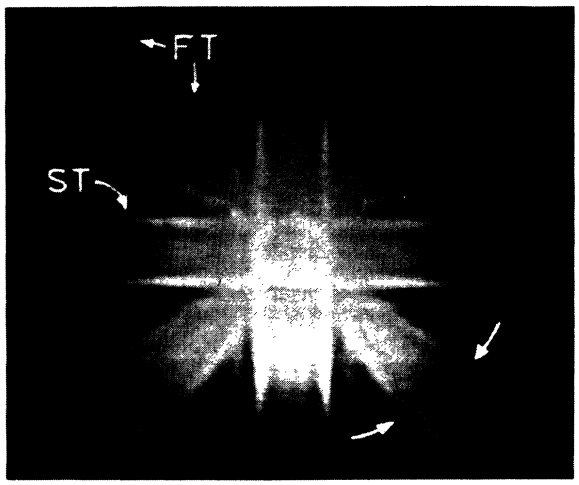

FIG. 21 Experimental phonon image of FT and ST phonons in the $In_{0.15}Ga_{0.85}As/AlAs$ SL described above, but for a detector cut-in frequency $\nu_c = 700$ GHz. The image was obtained with a fixed boxcar delay 50 ns wide at $t = 200$ ns after the laser pulse. A 25-μm Gaussian broadening due to finite laser-spot and detector resolution has been deconvolved from this image. The arrows indicate a Bragg scattering due to the SL.

the width of the transition is about 4°, as shown. Theoretically, the phonon stop band for this layer thickness is predicted to begin at about 48° and extend to 56°. The difference between the measured 43° and the predicted 48° may be attributed to corrections due to dispersion or uncertainty in the actual layer thickness.

The theoretical calculations in Figs. 9–11 suggest why

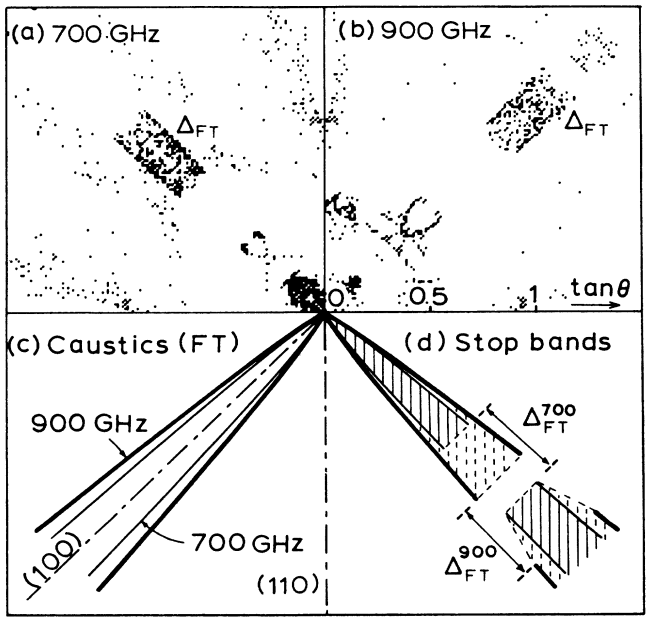

FIG. 22. Theoretical calculations used to explain Fig. 21. Parts (a) and (b) show the calculated spatial stop-band distributions for 700- and 900-GHz phonons, respectively. (c) Schematic of the FT caustics formed at 700 and 900 GHz. (d) Representation of the phonon stop-band effect for a range of frequencies, 700–900 GHz.

no ST stop-band effects were experimentally observed. For the experimental frequency range, ST stop bands occur either at large incident angles or else close to ⟨001⟩. If the Bragg condition occurs for small values of Θ, the stop bands occur throughout the intense ST focusing structure, and a reduction in the absolute intensity of this structure is difficult to distinguish.

VI. CONCLUSIONS

The secondary periodicity introduced by a superlattice is responsible for the Bragg reflection of acoustic phonons with experimentally accessible frequencies. In this paper we have examined the details of Bragg reflection of acoustic phonons in superlattices. Especially interesting is the intermode or coupled-mode Bragg reflection of phonons that can occur in addition to single-mode reflection. Bragg scattering yields frequency gaps—stop bands—in the phonon dispersion relation, occurring not only at the center and boundary of the folded Brillouin zone, but also inside the zone. In a real SL with a finite number of periods, exact periodicity does not exist, but calculations show significant dips in transmission for phonons with frequencies in the stop bands.

The phonon dispersion curves and the stop-band frequencies depend sensitively on the phonon-propagation direction. The angular distribution of the stop bands can be studied either with simple Bragg-condition maps or with Monte Carlo calculations of the phonon transmission. These two computational techniques reveal a rich variety of anisotropic structures due to both intramode and intermode Bragg scattering.

Phonon-imaging experiments on AlAs/GaAs and $In_xGa_{1-x}As/AlAs$ SL's generally confirm the validity of our theoretical predictions for the intramode and intermode Bragg processes. To observe the detailed features which are theoretically predicted, however, will require improved angular and frequency resolution. Such improvements are possible. The present experiments employ thin commercial substrates, which limit the angular resolution and require the use of higher detection frequencies (in order to exploit the high-frequency cutoff due to scattering). The phonon wavelengths at these high frequencies (700–850 GHz) are only a few lattice spacings, which favors the use of very thin SL layers. By using thicker substrates, the detection frequencies may be lowered and the SL layer thickness increased. It seems likely that the quality and characterization of the SL's will be improved under such conditions. Even with 20-Å-thick layers, however, we are able to observe fairly sharp features in the images due to Bragg reflection. For example, the principal zone-boundary stop band of L phonons appears as a distinct dip with ~6° width, corresponding to ≲150-GHz frequency spread, or ≲2-Å distribution in SL spacing.

Although we have concentrated on the GaAs SL's, the computational and experimental techniques we have developed are readily extended to other systems. Following the prediction of coupled-mode stop bands,[13] Santos *et al.*[14] have carried out phonon spectroscopy experiments at oblique angles with amorphous layers of Si and SiO_2, and they have observed extra stop bands that can

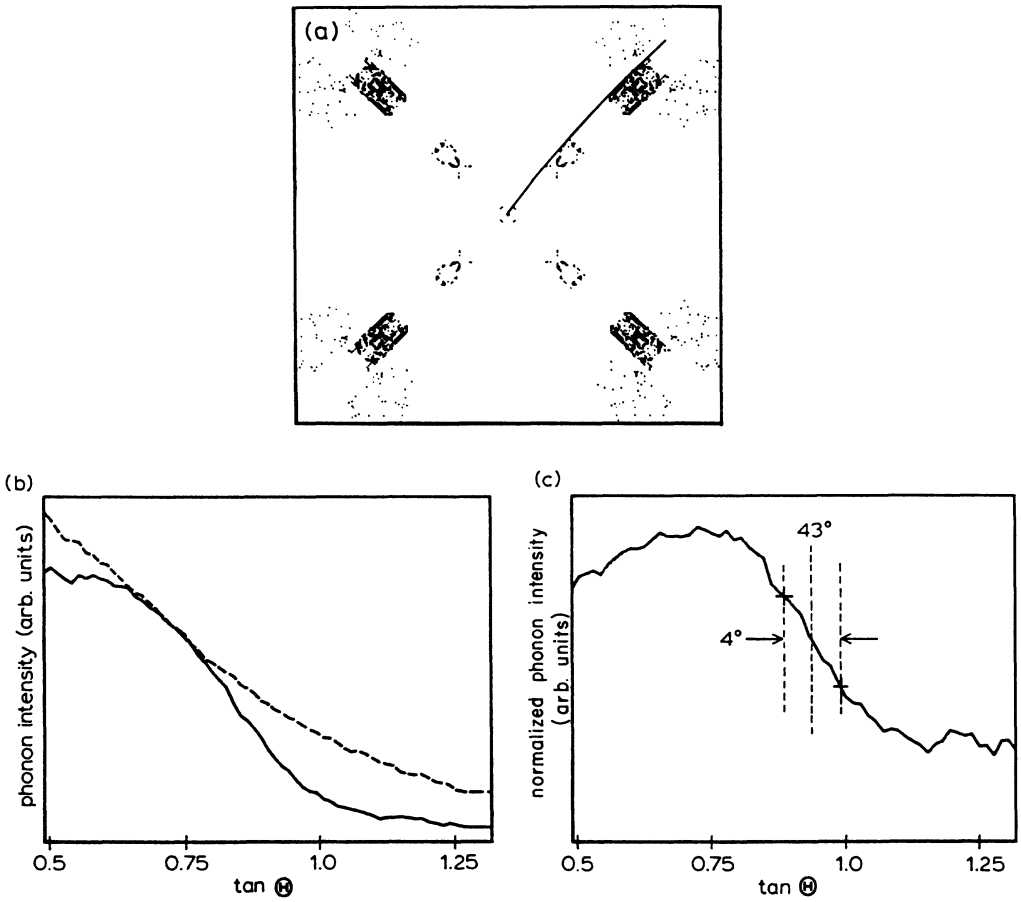

FIG. 23. FT-mode phonon stop-band effects. (a) Predicted stop-band distribution for an AlAs/GaAs SL with $d_A = d_B = 20$ Å and 20 periods, $\nu = 850$–900 GHz. The image scale is $\tan\Theta = \pm 1.5$. (b) Phonon transmission intensity vs Θ along the FT caustic, as indicated by the solid line in (a). The phonon intensity for the SL sample (solid line) and the substrate only (dashed line) are both shown. (c) Normalized SL transmission intensity (SL sample divided by substrate) along the FT caustic. The half-intensity point for the cutoff occurs at $\Theta \approx 43°$, with a width of about 4°.

be attributed to such processes. The angular dependence of phonon stop bands in these and other systems remains an interesting future problem.

ACKNOWLEDGMENTS

We are especially grateful to H. Morkoç for providing us with MBE superlattice samples, and to J. Chen and T. Henderson for help with sample preparation. Support for this work was provided by the U.S. National Science Foundation (NSF) under Grant No. DMR-86-12860. Equipment support was also provided by the NSF under Grant No. 85-21444. One of us (S.T.) acknowledges a travel grant by the Department of Education, Science and Culture of Japan.

*Permanent address: Department of Engineering Science, Hokkaido University, Sapporo 060, Japan.

[1]For recent reviews, see John M. Worlock, in *Proceedings of the 2nd International Conference on Phonon Physics,* edited by J. Kollár, N. Kroó, N. Menyhárd, and T. Siklós (World-Scientific, Singapore, 1985), p. 506; M. V. Klein, IEEE J. Quantum Electron. **QE - 22**, 1760 (1986).

[2]A. S. Barker, Jr., J. L. Merz, and A. C. Gossard, Phys. Rev. B **17**, 3181 (1978).

[3]J. Sapriel, J. C. Michel, J. C. Toledáno, R. Vacher, J. Kervarec, and A. Regreny, Phys. Rev. B **28**, 2007 (1983).

[4]C. Colvard, R. Merlin, M. V. Klein, and A. C. Gossard, Phys. Rev. Lett. **45**, 298 (1980); C. Colvard, T. A. Gant, M. V. Klein, R. Merlin, R. Fischer, H. Morkoç, and A. C. Gossard, Phys. Rev. B **31**, 2080 (1985).

[5]H. Brugger, G. Abstreiter, H. Jorke, H. J. Herzog, and E. Kasper, Phys. Rev. B **33**, 5928 (1986).

[6]S. M. Rytov, Akust. Zh. **2**, 71 (1956) [Sov. Phys.—Acoust. **2**, 68 (1956)].

[7]R. E. Camley, B. Djafari-Rouhani, L. Dobryzynski, and A. A. Maradudin, Phys. Rev. B **27**, 7318 (1983).

[8]S.-k. Yip and Y.-C. Chang, Phys. Rev. B **30**, 7037 (1984).

[9]M. J. Kelly, J. Phys. C **18**, 5963 (1985).

[10]V. Narayanamurti, H. L. Störmer, M. A. Chin, A. C. Gossard, and W. Wiegmann, Phys. Rev. Lett. **43**, 2012 (1979).

[11]O. Koblinger, J. Mebert, E. Dittrich, S. Döttinger, W. Eisenmenger, P. V. Santos, and L. Ley, Phys. Rev. B **35**, 9372 (1987).

[12]D. C. Hurley, S. Tamura, J. P. Wolfe, and H. Morkoç, Phys. Rev. Lett. **58**, 2446 (1987).

[13]S. Tamura and J. P. Wolfe, Phys. Rev. B **35**, 2528 (1987).

[14]P. V. Santos, J. Mebert, O. Koblinger, and L. Ley, Phys. Rev. B **36**, 1306 (1987).

[15]In numerical calculations, the following values were used: for AlAs—$\rho=3.76$ g/cm^3, $C_{11}=120.2$, $C_{12}=57.0$, and $C_{44}=58.9$ (all in units of 10^{10} dyn/cm^2); for GaAs—$\rho=5.36$ g/cm^3, $C_{11}=118.8$, $C_{12}=53.8$, and $C_{44}=59.4$ (all in units of 10^{10} dyn/cm^2); for $In_xGa_{1-x}As$—$\rho=5.36+0.31x$ g/cm^3, $C_{11}=118.8-32.0x$, $C_{12}=53.8-5.2x$, and $C_{44}=59.4-19.8x$ (all in units of 10^{10} dyn/cm^2). [See S. Adachi, J. Appl. Phys. **58**, R3 (1985); R. Reifenberger, M. J. Keck, and J. Trivisonno, *ibid.* **40**, 5403 (1969).]

[16]See, for example, B. A. Auld, *Acoustic Fields and Waves in Solids* (Wiley, New York, 1973).

[17]H. J. Maris, J. Acoust. Soc. Am. **79**, 906 (1971); B. Taylor, H. Maris, and C. Elbaum, Phys. Rev. B **3**, 1462 (1971); see also *Nonequilibrium Phonons in Nonmetallic Crystals*, Vol. 16 of *Modern Problems in Condensed Matter Sciences*, edited by W. Eisenmenger and A. A. Kaplyanskii (North-Holland, New York, 1986), p. 51.

[18]E. B. Christoffel, Annu. Mater. Pura Appl. **8**, 193 (1877); see also A. G. Every, Phys. Rev. Lett. **42**, 1065 (1979), Phys. Rev. B **22**, 1746 (1980).

[19]G. A. Northrop and J. P. Wolfe, Phys. Rev. B **22**, 6196 (1980).

[20]G. A. Northrop, Comput. Phys. Commun. **28**, 103 (1982).

[21]To determine the velocities and **k** vectors needed in the Bragg-condition maps, the *average* elastic constants and density for the AlAs/GaAs system were used.

[22]For a recent review of the phonon-imaging technique, see G. A. Northrop and J. P. Wolfe, in *Nonequilibrium Phonon Dynamics*, edited by W. E. Bron (Plenum, New York, 1985), p. 65.

[23]The superlattices were grown on 2-in.^{2} undoped GaAs wafers obtained from MA/Com, Inc., Metuchen, NJ. For each sample, the side opposite the superlattice was finished to optical quality with a Br:methanol etch.

[24]W. Eisenmenger, in *Physical Acoustics*, edited by W. P. Mason and R. N. Thurston (Academic, New York, 1976), Vol. 12, p. 79.

[25]K. H. Gundlach, S. Takada, M. Zahn, and H. J. Hartfusse, Appl. Phys. Lett. **41**, 294 (1982).

[26]S. Tamura, Phys. Rev. B **25**, 1415 (1982); **28**, 897 (1983).

[27]W. Dietsche, G. A. Northrop, and J. P. Wolfe, Phys. Rev. Lett. **47**, 660 (1980); G. A. Northrop, S. E. Hebboul, and J. P. Wolfe, *ibid.* **55**, 95 (1985).

[28]S. E. Hebboul and J. P. Wolfe, Phys. Rev. B **34**, 3948 (1986).

[29]V. Narayanamurti, M. A. Chin, and R. A. Logan, Appl. Phys. Lett. **33**, 481 (1978).

[30]S. Tamura and T. Harada, Phys. Rev. B **32**, 5245 (1985).

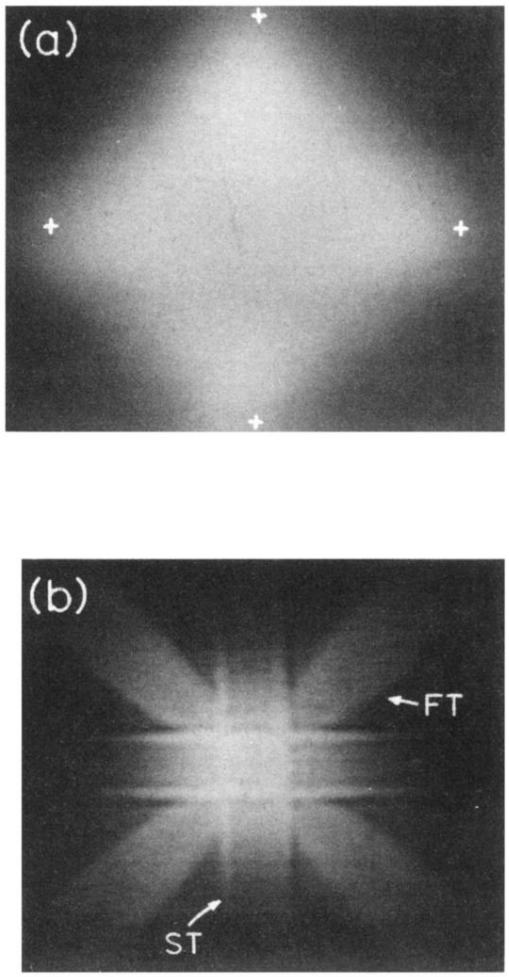

FIG. 13. Experimental phonon images of the phonon flux intensity in an (001)-oriented GaAs substrate. (a) Constant-velocity image of L phonons ($v = 5.4$ km/s). The image is centered on the [100] direction, and spans approximately $\pm 60°$ left to right. Adjacent $\langle 111 \rangle$ directions are indicated by the crosses. (b) Constant-delay image (gate 80 ns wide at $t = 230$ ns after the laser pulse) of FT- and ST-phonon intensities. The bright lines of high flux intensity (caustics) are due to phonon focusing. A 25-μm Gaussian broadening due to finite laser-spot and detector resolution has been deconvolved from this image.

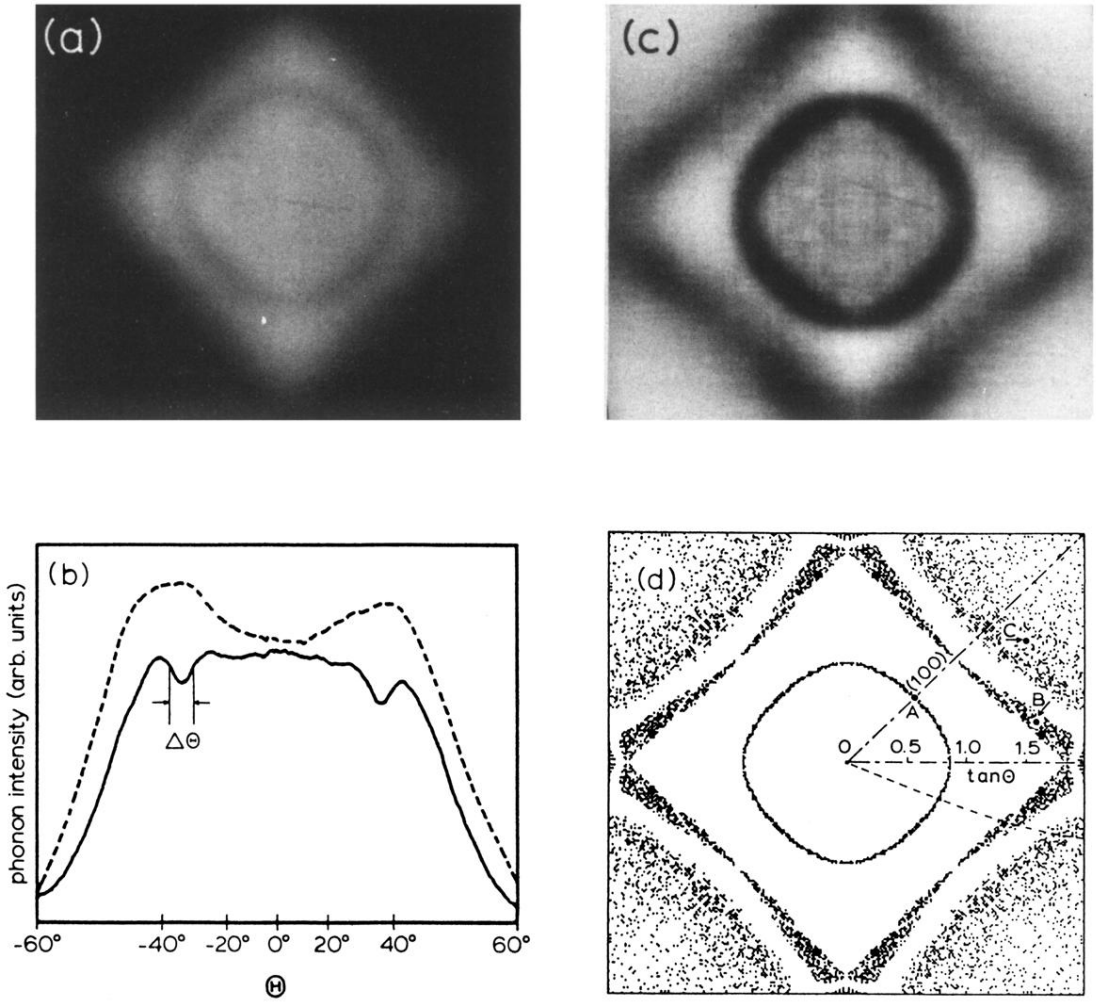

FIG. 14. Phonon images for a (001) $In_{0.15}Ga_{0.85}As/AlAs$ SL with $d_A = d_B = D/2 = 20$ Å and 40 periods. (a) Experimental constant-velocity image of L phonons ($v = 5.4$ km/s). The image scale and orientation are approximately the same as in Fig. 13(a). (b) Scan of phonon intensity across the center of the image for the SL sample (solid line) and the substrate sample (dashed line). The relative intensities of the two curves is arbitrary for display purposes. (c) Difference image created by subtracting the substrate image of Fig. 13(a) from the SL-plus-substrate image in (a), shown at increased gain. To improve the signal-to-noise ratio, the four symmetry-related quadrants have been averaged. (d) Calculated stop-band distribution for L phonons in this system. The dashed line and points A, B, and C are for reference in Figs. 15 and 16.

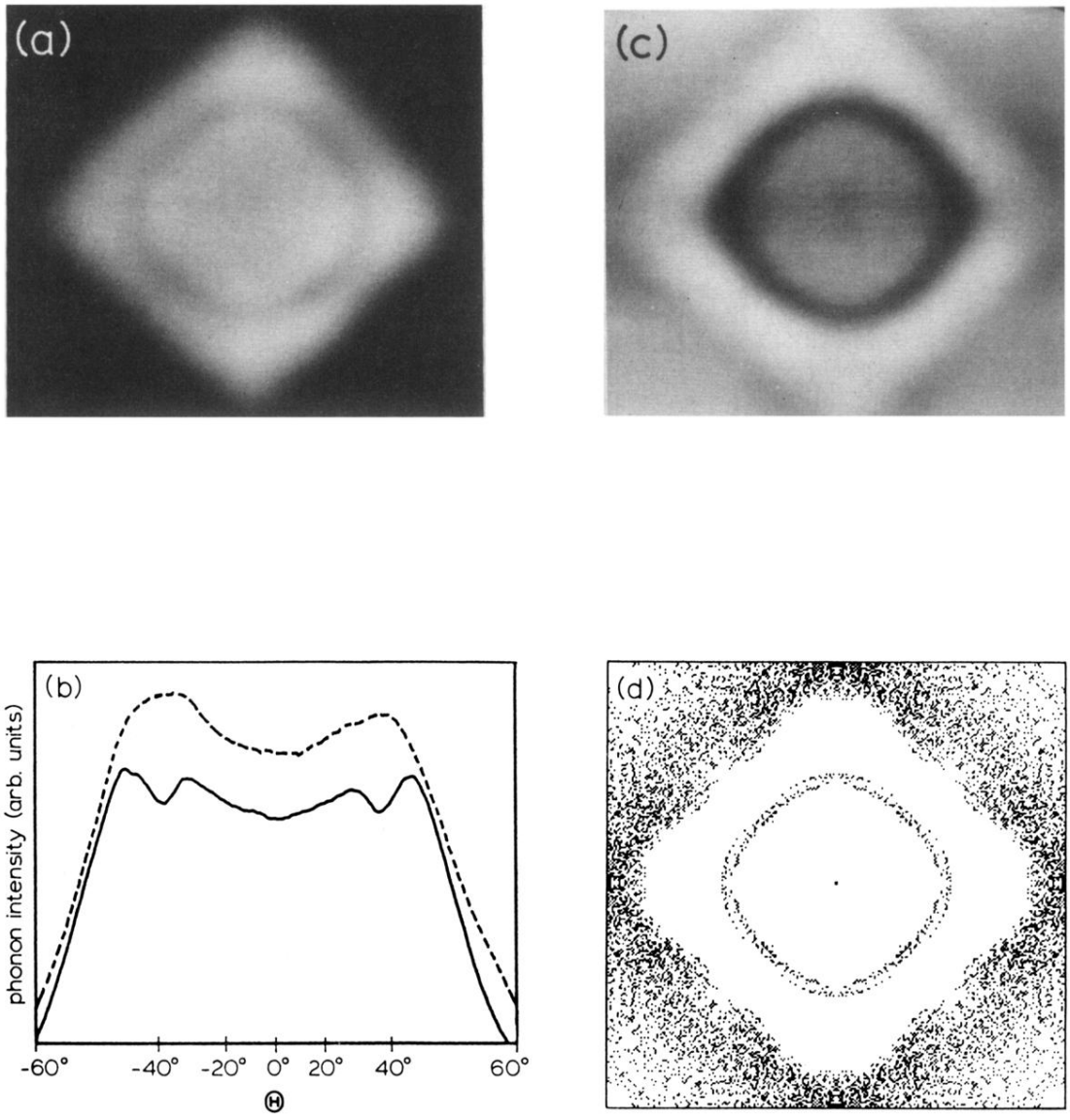

FIG. 18. Phonon images for a (001) $In_{0.25}Ga_{0.75}As/AlAs$ SL with $d_A = d_B = 20$ Å and 40 periods. (a) Experimental constant-velocity phonon image of L phonons ($v = 5.4$ km/s). The image scale and orientation are the same as in Fig. 13(a). (b) Intensity scan across central line in image in (a) (solid line) and substrate sample (dashed line). (c) Difference image, shown with the same amplification as the image in Fig. 14(c). (d) Calculated image of L-mode stop-band distribution for $\nu = 850$–950 GHz.

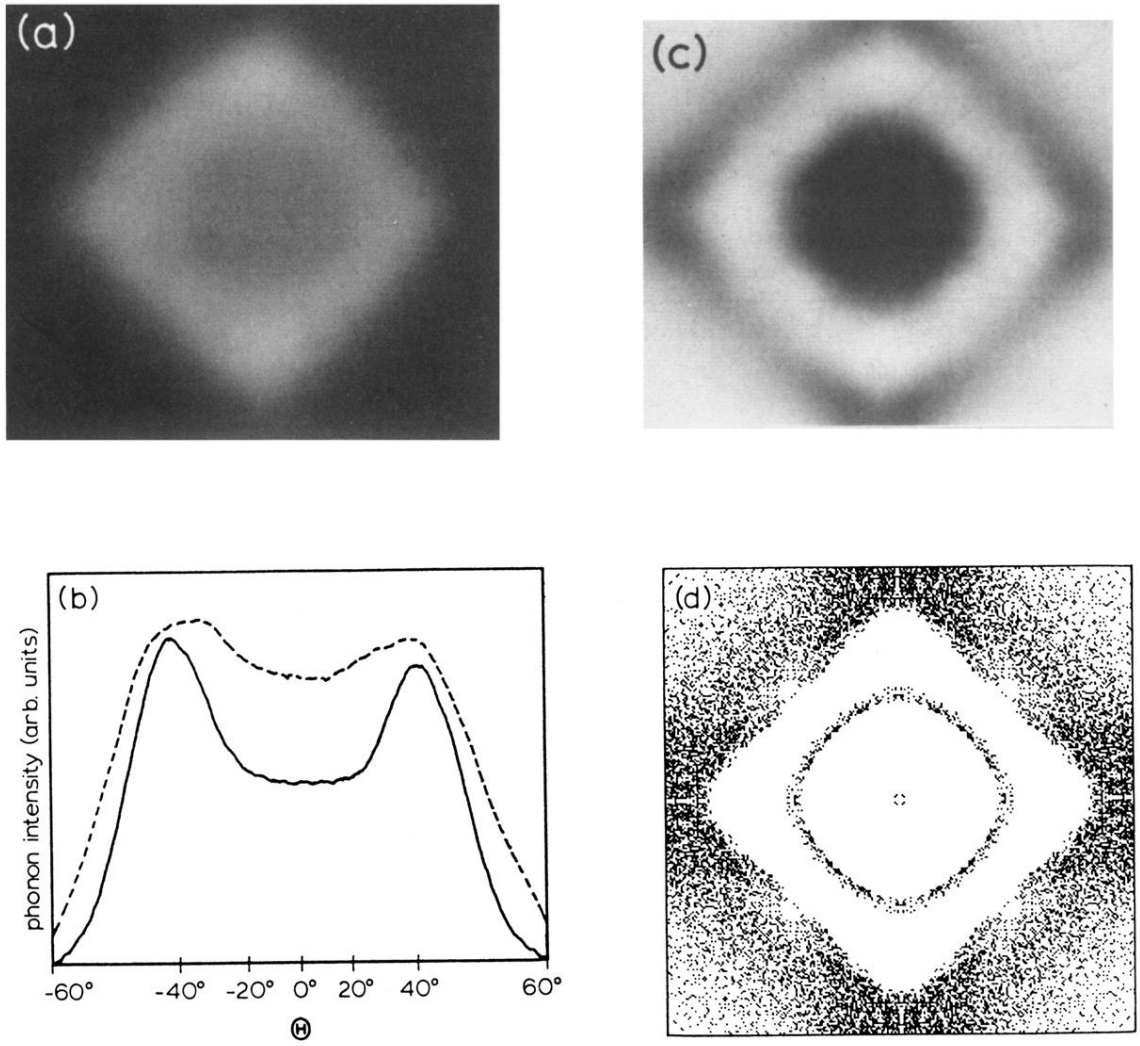

FIG. 19. Experiment and theory for L phonons in an AlAs/GaAs SL with $d_A = d_B = 20$ Å and 20 periods. (a) Experimental constant-velocity phonon image ($v = 5.4$ km/s). Image scale and orientation are approximately the same as in Fig. 13(a). (b) Intensity across scan line in center of (a) (solid line) and substrate (dashed line). (c) Difference image. (d) Theoretically predicted stop-band distribution for L phonons, $\nu = 850$–950 GHz.

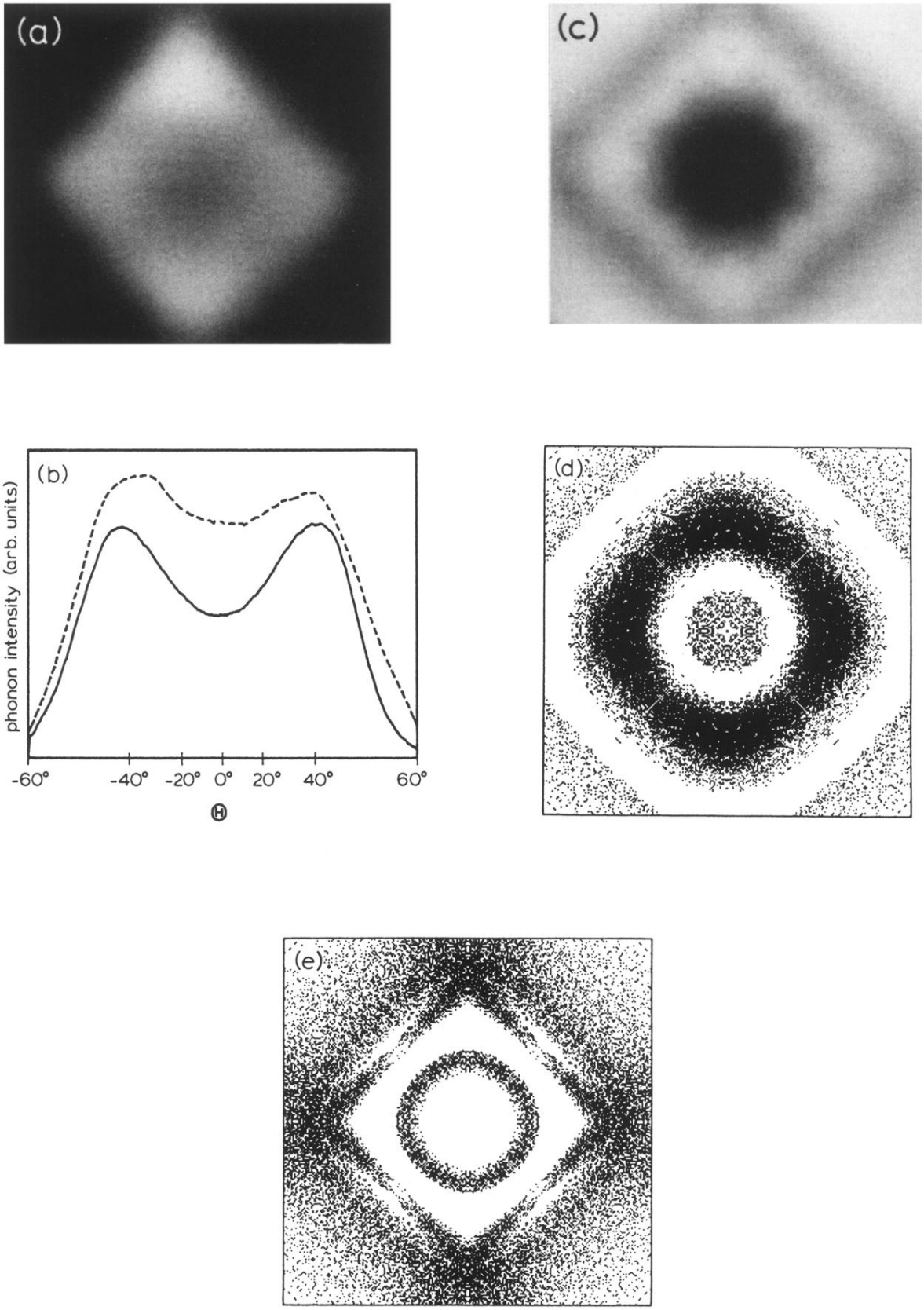

FIG. 20. (a) Experimental constant-velocity image ($v = 5.4$ km/s) for L phonons in an AlAs/GaAs SL with $d_A = d_B = 15$ Å and 40 periods. The image scale and orientation are the same as in Fig. 13(a). (b) Intensity vs position for line across center of (a) (solid line) and substrate sample (dashed line). (c) Difference image. (d) Calculated spatial stop-band distribution ($\nu = 850$–950 GHz) for an AlAs/GaAs SL with $d_A = d_B = 14$ Å, corresponding to five atomic monolayers. (e) Predicted distribution of L-mode stop bands for an AlAs/GaAs SL with $d_A = d_B = 17$ Å, corresponding to six atomic monolayers.

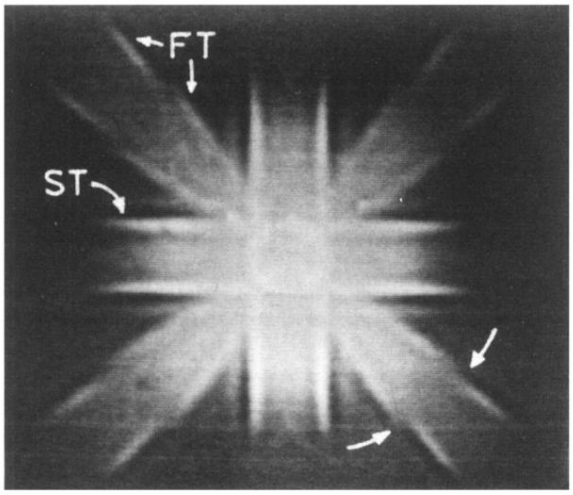

FIG. 21 Experimental phonon image of FT and ST phonons in the $In_{0.15}Ga_{0.85}As/AlAs$ SL described above, but for a detector cut-in frequency $\nu_c = 700$ GHz. The image was obtained with a fixed boxcar delay 50 ns wide at $t = 200$ ns after the laser pulse. A 25-μm Gaussian broadening due to finite laser-spot and detector resolution has been deconvolved from this image. The arrows indicate a Bragg scattering due to the SL.